

A New Class of Materials Based on Nanoporous High Entropy Alloys with Outstanding Properties

Author names and affiliations:

Jarod Worden^a, Celine Hin^{a,b}, Juergen Biener^c

a. ME department

Northern Virginia Center, Virginia Polytechnic Institute
7054 Haycock Rd, Falls Church, VA 22043, United States

b. MSE department

Northern Virginia Center, Virginia Polytechnic Institute
7054 Haycock Rd, Falls Church, VA 22043, United States

c. Materials Science Division

Physical and Life Sciences Directorate
Lawrence Livermore National Laboratory
Livermore, CA 94550

Corresponding Author

E-mail address: jaworden@vt.edu (Jarod Worden)

Postal Address: Northern Virginia Center, Virginia Polytechnic Institute
7054 Haycock Rd, Falls Church, VA 22043, United States

Abstract

Nanoporous metals with a random, bicontinuous structure of both pores and ligaments exhibit many unique mechanical properties, but their technical applications are often limited by their intrinsic brittleness under tensile strain triggered by fracture of the weakest ligaments. Here, we use molecular dynamics simulations to study the mechanical behavior and thermal stability of two different bicontinuous nanoporous high entropy alloys, $\text{Al}_{0.1}\text{CoCrFeNi}$ and NbMoTaW . To isolate the properties related to the nanoporous nature of our samples, we also studied the corresponding bulk and nanocrystalline systems. The results demonstrate that the specific modulus of nanoporous HEAs are 2 to 3 times greater than that of single element nanoporous materials with specific strength reaching values 5 to 10 times higher, comparable to bulk metals with the highest specific strength. Bicontinuous HEAs also displayed excellent resistance to thermal degradation as evidenced by the absence of coarsening ligaments up to temperatures of 1273 K which ensures the durability and reliability in high-temperature applications. The findings uncover unprecedented mechanical and thermal properties of bicontinuous nanoporous high entropy alloys, paving the way for their promising utilization in advanced engineering and structural applications.

1. Introduction

Nanoporous metals with a random, bicontinuous structure exhibit a unique combination of mechanical properties such as high stiffness, low specific density, high compression strengths, and excellent energy absorption capabilities¹. However, one of the biggest hurdles for nanoporous materials is the brittleness under strain conditions due to the catastrophic failure of the material triggered by fracturing of the weakest ligaments leading to the overloading and fracture of adjacent ligaments^{2,3}. Gold, a commonly studied nanoporous material, has shown promise in deformation analysis through molecular dynamics simulations and experimental investigations, particularly in applications related to sensors and actuators^{4,5}. The molecular dynamics simulations on nanoporous amorphous alloy Cu₅₀Zr₅₀ alloy performed by Zhang reveal the typical failure mechanism consisting of a cascade of ligament necking and fracturing once ultimate stress is achieved⁶. To address the brittleness issue of nanoporous metals caused by cascading ligament failures, we decided to study materials with high strain hardening that we expect to protect nanoporous structures from fracturing by reducing the probability of single ligament failure. One class of materials that provides significant strain hardening is that of High Entropy Alloys (HEAs)^{7,8}. HEAs utilize multiple equiatomic concentrations of elements to increase the entropy of the system, thus stabilizing disordered solid-solution phases while suppressing the formation of brittle intermetallic phases^{1,9}. This allows for HEAs to benefit from the properties of the multiple components including the potential for high strength and hardness, high fatigue, creep, wear resistance, and high strain hardening^{9,10}. Incorporating a bicontinuous nanoporous structure is expected to further increase the potential of HEAs for enhanced mechanical properties beyond those of traditional metals and alloys, thus making this material a promising candidate for highly demanding applications.

This paper focuses on utilizing Molecular Dynamics (MD) simulations of nanoporous HEAs and studying the mechanical response under uniaxial compression and tensile testing which are then compared to the corresponding mechanical properties of bulk and polycrystalline HEAs. Al_{0.1}CoCrFeNi and NbMoTaW HEAs were selected due to their single disordered face-centered cubic (fcc) phase and body-centered cubic (bcc) phase, respectively, as opposed to other HEAs that may have multiple or ordered phases¹¹. The simulation results confirm our hypothesis that nanoporous HEAs possess unique properties compared to other materials with high specific strength and low specific Young's modulus. The phase space with respect to weight-normalized Young's modulus and yield strength of different classes of materials is illustrated in Fig. 1 with the red circle indicating the general phase space occupied by single component nanoporous materials based on available data. The results for nanoporous Al_{0.1}CoCrFeNi and NbMoTaW are indicated by the red and blue boxes demonstrating that these materials exhibit higher specific strength and specific modulus values compared to typical single-component nanoporous materials as well as possessing high specific strength to Young's modulus ratio compared to traditional metals. Typical materials used in industry include steel, aluminum, magnesium, copper, titanium, composites, and plastics that frequently have limitations in their applications due to high density or low thermal tolerance^{12,13}. The results of our simulations suggest that these particular nanoporous HEAs outcompete many of the materials displayed, including being lighter at the particular relative densities studied compared to other low-density

materials like titanium. Such lightweight materials with high strength promise societal and industrial impacts for high energy absorption applications. For high energy absorption/impact resistant materials, the mechanical properties of high strength and low modulus are necessary to maximize energy deflection and allowable stress¹⁴. This transformative concept of nanoporous HEAs will benefit many industries, including nuclear, automotive, aerospace, and aeronautics. For example, replacing steels by nanoporous $\text{Al}_{0.1}\text{CoCrFeNi}$ in vehicle design can reduce the average weight by 50%, lowering oil consumption and decreasing CO_2 emissions by 40% (more details are provided in the supplemental information under Supplementary Discussion 1). Finally, the exceedingly high density of nanopores leads to a high surface-to-volume ratio that is expected to provide unusually high radiation tolerance as surfaces act as unsaturable, perfect sinks for defects. This self-healing property makes nanoporous HEAs promising candidates for the next generation of nuclear reactors, for example, using NbMoTaW for additional shielding due to its high helium radiation resistance¹⁵⁻¹⁸.

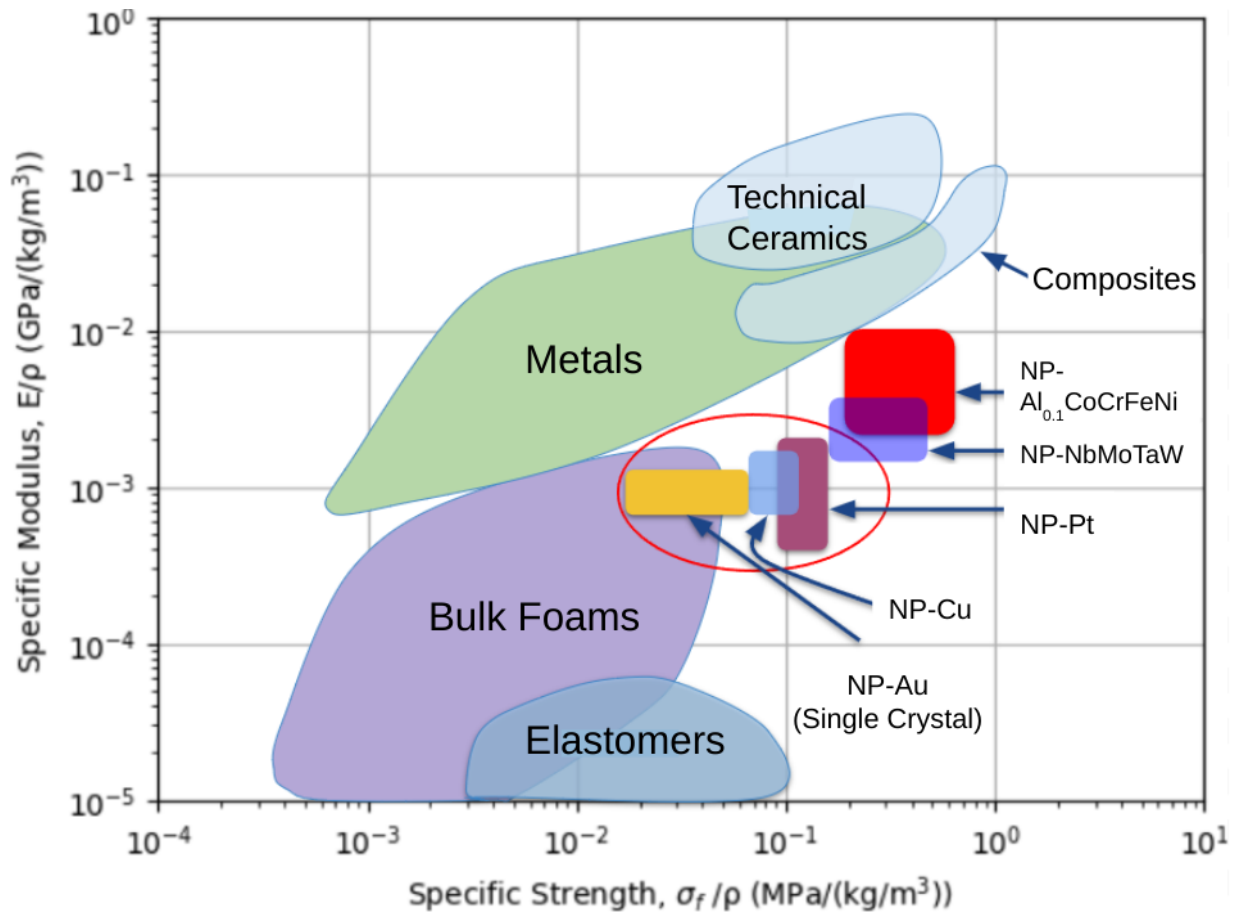


Figure 1. Weight-normalized Young’s modulus and yield strength for different classes of materials including bulk materials and nanoporous materials¹⁹. The red box represents the nanoporous HEA $\text{Al}_{0.1}\text{CoCrFeNi}$ and the blue box represents the nanoporous HEA NbMoTaW (color in print).

2. Results

MD simulations were used to perform mechanical compression and tensile tests at 298/600/1273 K. A Nose/Hoover thermostat and barostat (NPT) ensemble with damping parameters of 0.1 picoseconds for temperature and pressure control was first used for 100.0 ps for thermalization at the studied temperature and atmospheric pressure until the lattice parameter and energy of the system reached a steady state. After thermalization, the NPT ensemble is maintained and a strain rate of 10^9 s^{-1} is imposed to deform the simulation box along the [100] direction from 0-75% strain for compression tests and 0-50% strain for tensile tests. The large strain rate is a limitation of the small-time scales of MD simulations where realistic strain rates would take an unrealistically long time to simulate. The types of systems that were examined are shown in Fig. 2 and the methods of constructing each structure is described in the Methods section of the Supplementary materials file.

2.1 Stress-Strain curve analysis

The results of the mechanical tests at 600 and 1273 K of the $\text{Al}_{0.1}\text{CoCrFeNi}$ and NbMoTaW systems demonstrate the exceptional mechanical properties of nanoporous High-Entropy Alloys (Fig. 3 and Fig. 4) (the corresponding results from the 298 K tests are shown in the supplementary information section under Fig. S1 and Fig. S2). The yield strength and Young's modulus for the 298 and 1273 K systems are summarized in tables 1-4. The information in tables 1 and 3 are extrapolated from Fig. S1 and S2 in the supplementary information section. Independent of temperature, all $\text{Al}_{0.1}\text{CoCrFeNi}$ systems exhibit a linear elastic behavior in the low strain region of 0-2%. For non-nanoporous structures, an increasing strain starts to display non-linear elastic deformation until the ultimate stress is reached at 5% strain. Tensile testing displays higher strain values corresponding to ultimate stress for nanoporous $\text{Al}_{0.1}\text{CoCrFeNi}$ compared to the bulk and nanocrystalline systems. For the bulk systems, the yield strength is reached early compared to the ultimate strength at higher strains, signifying the strain-hardening mechanism of the HEAs¹⁰. For the nanocrystalline systems under both compression and tension, the stress drops significantly after reaching the yield peak followed by a plateau region up to the highest strain values. The primary difference between tensile and compression tests for the nanocrystalline systems is that higher stress values are reached under compression compared to the tensile tests. This compression-tension asymmetry of the yield strength in bulk and polycrystalline $\text{Al}_{0.1}\text{CoCrFeNi}$ has also been reported for other HEA systems²⁰ and probably reflects different deformation mechanisms, such as twinning in compression and slip in tension²¹.

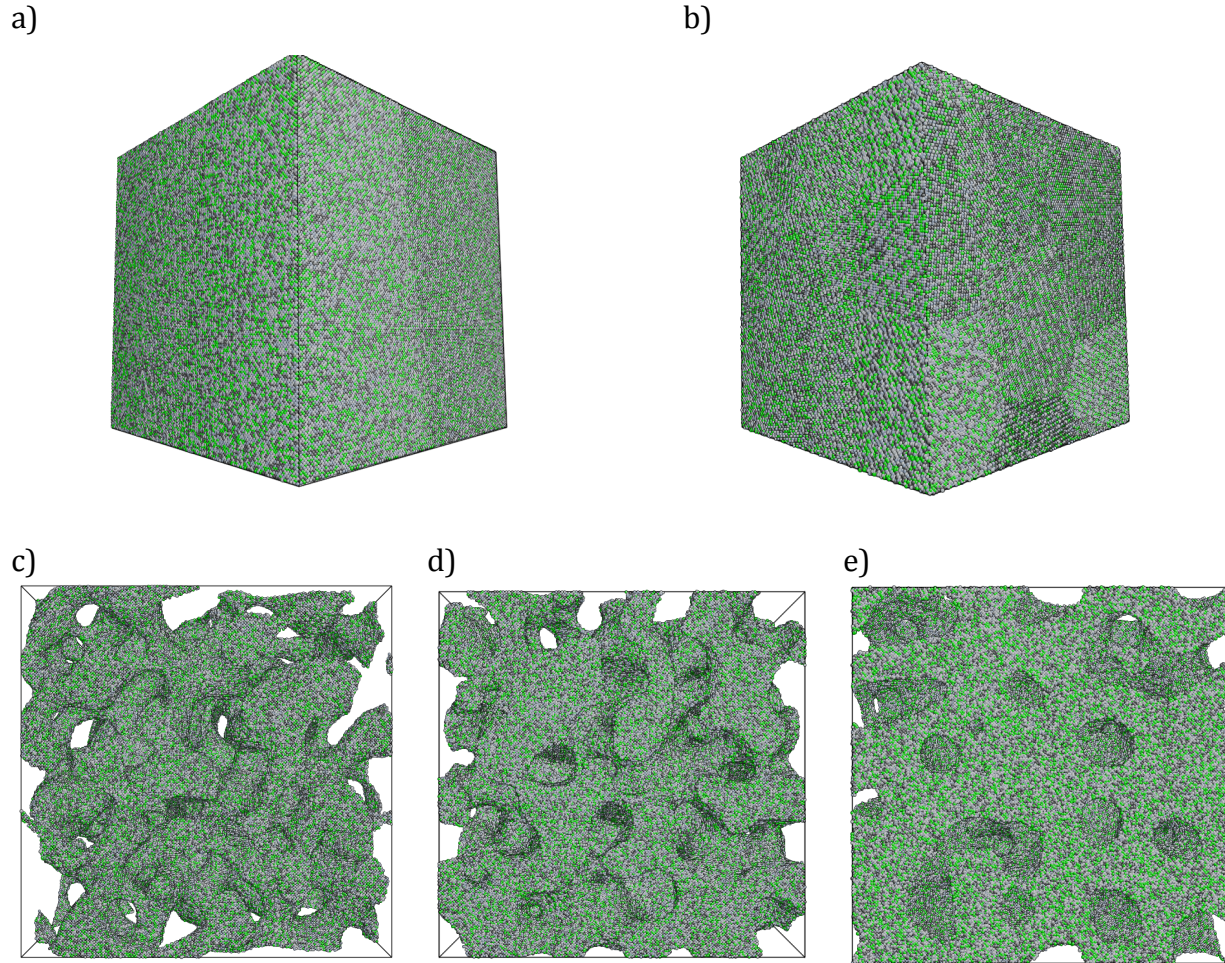


Figure 2. The simulation boxes of the HEA $\text{Al}_{0.1}\text{CoCrFeNi}$ systems for (a) bulk, (b) 30 nm polycrystalline, and (c, d, e) nanoporous $\text{Al}_{0.1}\text{CoCrFeNi}$ with relative densities of 28.7 (c), 47.8 (d), and 67.2% (e), respectively (color in print).

Compared to the bulk and nanocrystalline systems, nanoporous $\text{Al}_{0.1}\text{CoCrFeNi}$ displayed more complex responses to both tests. In compression tests, only a very small yield peak is observed for the highest relative densities, and the stress plateaus immediately after reaching the yield stress followed by a region where the stress gradually increases with increasing strain. This is a common response of many nanoporous systems under uniaxial compression for experiments and simulations²². When comparing ligament sizes to similar relative densities, smaller ligaments had lower yield stresses compared to larger ligaments, but surpassed larger ligaments stress values at higher strains. By contrast, tensile tests of nanoporous $\text{Al}_{0.1}\text{CoCrFeNi}$ show a more pronounced yield peak followed by a shorter plateau before the stress starts to decrease with further increasing strain. Exceptions are the nanoporous $\text{Al}_{0.1}\text{CoCrFeNi}$ sample with the smallest ligaments: The sample with the smallest ligaments (2.57 nm) shows no yield peak but a steady increase in stress with increasing strain very similar to the corresponding compression test: The sample with 3.04 nm ligaments shows a small yield peak followed by a log plateau similar to the bulk

nanocrystalline samples. $\text{Al}_{0.1}\text{CoCrFeNi}$ systems are also dependent on temperature with higher temperatures leading to lower stresses for all the systems. This can be seen with the bulk and nanocrystalline systems displaying the sharpest decrease in stress for increasing temperature. Lower relative density systems have a smaller reduction in stress compared to the higher relative density system with increasing temperature. This suggests that lower relative density nanoporous $\text{Al}_{0.1}\text{CoCrFeNi}$ have a higher resistance to thermal coarsening of ligaments compared to higher relative density systems that reduces the overall strength of nanoporous materials. Typically, nanoporous systems undergo coarsening which increases the average ligament and pore size, thus decreasing strength²³. The smaller ligament systems with similar relative densities have a greater reduction in stress compared to the larger ligament systems for increasing temperatures. This could potentially be attributed to higher temperatures causing thermal instability in the smallest ligaments leading to higher rates of ligament failure. This process occurred in the 28.7% relative density, 2.2 nm ligament size system where the mechanical testing at other temperatures outside of the room temperature environment would lead to the collapse of the ligament structure during the initial relaxation phase, quickly collapsing and reducing the simulation box geometry.

The NbMoTaW systems (Fig. 4) undergo similar stress-strain trends as the $\text{Al}_{0.1}\text{CoCrFeNi}$ systems with an initial increase of stress and a more or less pronounced yield peak at about 5% strain, followed by a plateau region where the stress stays about constant with increasing strain. Under tensile strain, the stress of the bulk NbMoTaW system is shown to oscillate after failure strain, which is represented by the oscillating atomic positions of the atoms after a rupture of the system. Increasing temperature also shows a decrease in stress across all systems, with greater stress reduction for bulk and nanocrystalline structures. With the nanoporous structures, higher relative density systems displayed a larger decrease in stress compared to the lower relative density systems with increasing temperature as was observed in the $\text{Al}_{0.1}\text{CoCrFeNi}$ nanoporous structures. The mechanical properties for NbMoTaW display higher values compared to $\text{Al}_{0.1}\text{CoCrFeNi}$ systems, such as the yield strength and Young's modulus. This is due to the individual elements of the NbMoTaW system possessing higher yield strength, ultimate strength, and Young's modulus for compression and tensile environments compared to the individual elements of the $\text{Al}_{0.1}\text{CoCrFeNi}$ HEA²⁴. A more thorough analysis of yield strength and Young's modulus, such as asymmetries and comparisons to literature, is supplied in Supplementary Discussion 2.

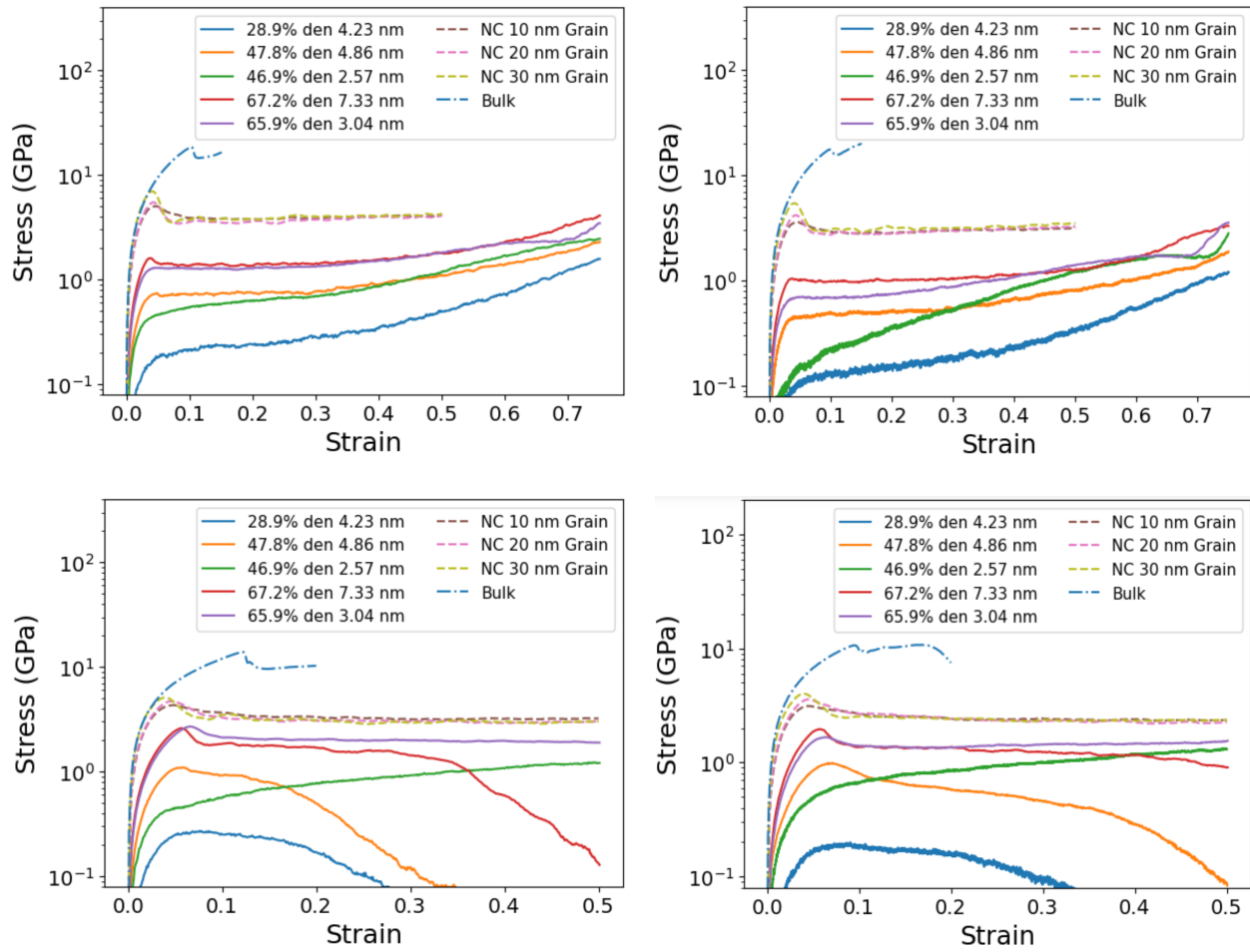


Figure 3. Stress strain curves of compression (top row) and tensile (bottom row) tests for $\text{Al}_{0.1}\text{CoCrFeNi}$ systems at 600 K (left column)/1273 K (right column). NC represent nanocrystalline systems (color in print).

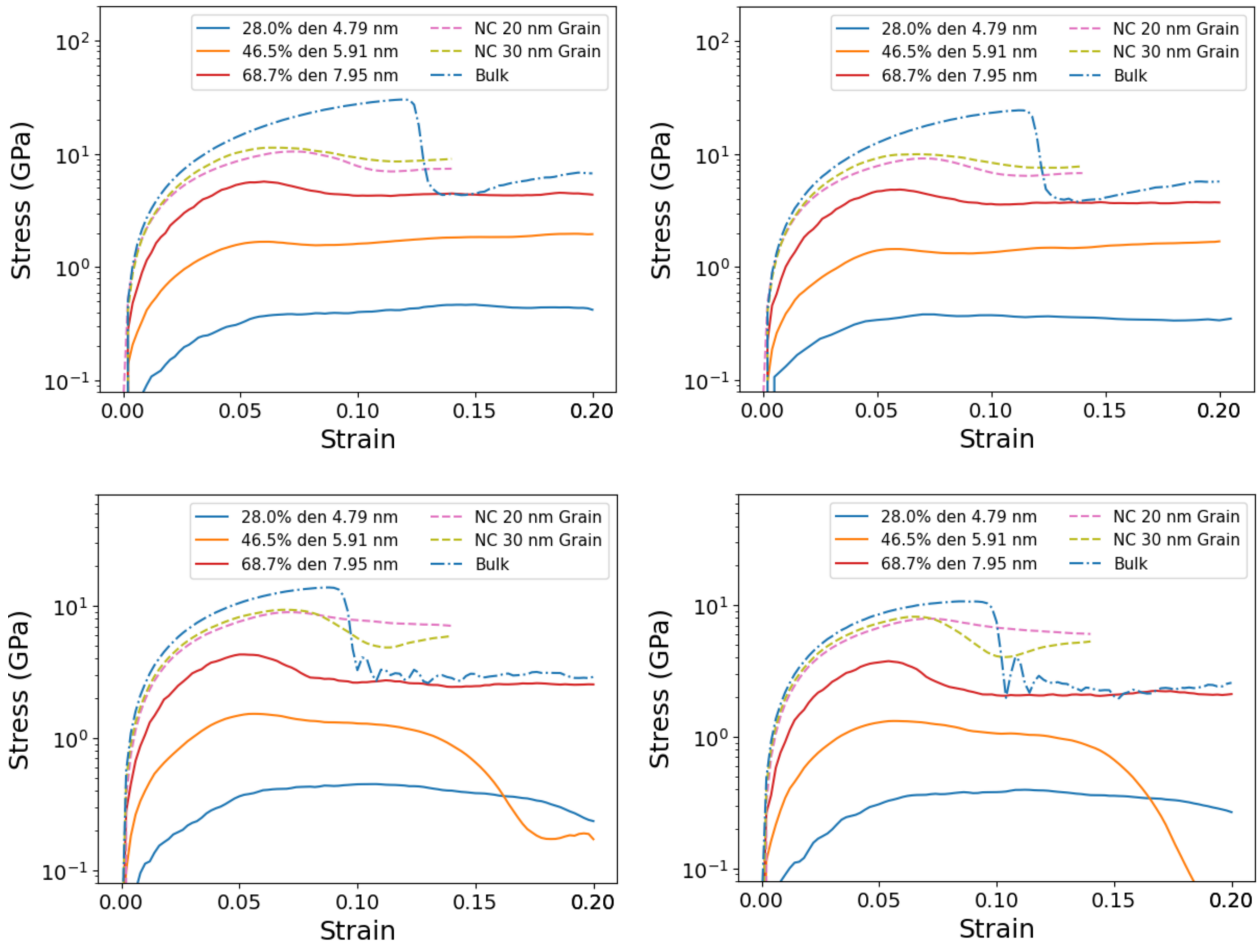


Figure 4. Stress strain curves of compression (top row) and tensile (bottom row) tests for NbMoTaW systems at 600 K (left column) / 1273 K (right column). NC represents nanocrystalline systems (color in print).

Table 1. Young's modulus and yield strength in GPa of the analyzed Al_{0.1}CoCrFeNi HEA systems at 298 K. Experimental and other simulation results are in parentheses. All units are in GPa.

System	Young's Modulus Tension	Young's Modulus Compression	Yield Strength Tension	Yield Strength Compression
Bulk	199.82 (199, 203 ^{25,26})	254.15 (260 ²⁶)	6.81 (6.48 ²⁶)	8.12 (7.86 ²⁶)
10 nm grain	165.96	180.91	3.32	3.98
20 nm grain	168.70	182.52	3.37	4.75
30 nm grain	200.91	236.15	4.42	6.61
28.9% density 4.23 nm	6.01	4.84	0.28	0.21
28.7% density 2.20 nm	5.67	2.71	0.26	0.12
47.8% density 4.86 nm	26.75	23.84	1.09	0.79
46.9% density 2.57 nm	23.68	17.08	0.90	0.54
67.2% density 7.33 nm	57.15	54.37	2.46	1.85
65.9% density 3.04 nm	52.60	45.98	2.38	1.47

Table 2. Young's modulus and yield strength in GPa of the analyzed Al_{0.1}CoCrFeNi HEA systems at 1273 K. All units are in GPa.

System	Young's Modulus Tension	Young's Modulus Compression	Yield Strength Tension	Yield Strength Compression
Bulk	187.31	226.24	4.31	5.21
10 nm grain	116.36	126.12	2.09	3.89
20 nm grain	122.23	130.40	2.20	3.78
30 nm grain	164.24	177.56	2.63	3.91
28.9% density 4.23 nm	3.78	2.67	0.12	0.07
28.7% density 2.20 nm	-	-	-	-
47.8% density 4.86 nm	15.67	14.84	0.97	0.40
46.9% density 2.57 nm	10.72	2.50	0.43	0.14
67.2% density 7.33 nm	38.20	32.60	1.91	1.04
65.9% density 3.04 nm	32.24	21.89	1.48	0.66

Table 3. Young's modulus and yield strength in GPa of the analyzed NbMoTaW HEA systems at 298 K. All units are in GPa.

System	Young's Modulus Tension	Young's Modulus Compression	Yield Strength Tension	Yield Strength Compression
Bulk	252.50 (245 ²⁷)	309.82 (300 ²⁸)	10.10	39.67
20 nm grain	191.29	205.16	6.12	8.21
30 nm grain	193.75	221.41	6.86	10.15
28.0% density 4.79 nm	7.45	6.15	0.41	0.43
46.5% density 5.91 nm	38.41	35.57	1.31	1.85
68.7% density 7.95 nm	110.27	122.42	3.97	5.63

Table 4. Young's modulus and yield strength in GPa of the analyzed NbMoTaW HEA systems at 1273 K. All units are in GPa.

System	Young's Modulus Tension	Young's Modulus Compression	Yield Strength Tension	Yield Strength Compression
Bulk	190.05	246.99	7.37	21.24
20 nm grain	164.14	177.94	4.94	6.41
30 nm grain	170.77	200.97	6.15	8.40
28.0% density 4.79 nm	5.29	5.23	0.34	0.36
46.5% density 5.91 nm	30.29	28.18	1.21	1.47
68.7% density 7.95 nm	90.13	100.17	3.06	4.41

2.2 Fracture Analysis in Tensile Tests of Nanoporous Al_{0.1}CoCrFeNi

Fracture analysis was only performed on tensile test specimens as fracturing was not observed in compression tests that are dominated by ligament bending as the primary deformation mode²⁹. The system being examined is a section of the 28.9% relative density, 4.23 nm ligament system under 1273 K tensile testing and was analyzed using the Dislocation Extraction Algorithm (DXA) with Paraview^{30,31}. The surface topography is shown as a blue opaque surface that delineates the surface atoms (Fig.4a). This surface can then be turned into a mesh to observe the defects in the system. Fig. 4b-d shows dislocations, twin boundaries, and stacking faults in the ligament under investigation at different strains during fracturing. Dislocations are observed during the initial stage of fracturing but are not prominent during ligament failure (Fig.4b). Twin boundaries also form during the initial stage of fracturing and remain present during ligament failure but easily break apart as the ligament fractures (Fig.4c). Stacking faults are the most prominent defects observed and heavily populate the ligament through all stages of the fracturing process (Fig.4d). The high number of stacking faults in the fracture process is a consequence of the HEA system's low stacking fault energy (SFE). The SFE of the bulk system was calculated to be 32.777 mJ/m², which is in good agreement with the experimental value of 30 mJ/m² and with other computational results^{32,33}. This differentiates the fracture processes of HEA ligaments from that observed in the ligaments of nanoporous Au^{5,34,35}. In the beginning of the fracture process, the nanoporous HEAs follow similar defect mechanisms of stacking fault and partial dislocation formation in the ligament³⁴. However, the deformation mechanism of nanoporous HEA deviates at higher strains where, due to a lack of dislocations, stacking faults become the primary defect observed when the ligament breaks³⁴. By contrast, dislocations appear to play a key role in the deformation of the Au ligaments, either through large dislocation pileups that cause a

saturation of formed stacking faults, or through dislocation mediated shearing^{5,35}. The lack of distinct dislocations in the HEA system could be caused by 1) the impediment of dislocation motion due to lattice distortion by the different atomic species in the HEA material that is expected to reduce the formation of larger dislocations and 2) the large amount of stacking faults impeding dislocations³⁶. Due to the primary dislocation type being partial dislocations, neighboring partial dislocations formed in the ligament would create a highly stable stacking fault between them due to the lower dissociation of the partial dislocations from impaired mobility in the nanoporous HEA system, decreasing the number of standalone dislocations³⁷. As dislocation motion is typically a primary mechanism for plastic deformation, a lack of dislocations requires the presence of a separate process for the fracturing of the ligaments during uniaxial tension^{38,39}. Due to the high number of stacking faults populating the ligament structure during the fracturing, the primary process is most closely related to the twinning mechanism in fcc metallic materials that is most prominent during severe plastic deformation⁴⁰. This is the most common deformation mechanism observed during tensile tests.

2.3 Fracture Analysis in Tensile Tests of Nanoporous NbMoTaW

In contrast to the prevalence of dislocations, stacking faults, and twin boundaries in the nanoporous $\text{Al}_{0.1}\text{CoCrFeNi}$, NbMoTaW is lacking many of the same defects in the ligaments during the fracturing process (Fig S3). The only defects are dislocations observed at 15% strain located at the end segment of the ligament, when the notch in the center of the ligament forms. No other defects were observed at lower or higher strain values, implying more complex defects influencing the fracture mechanism. The lack of stacking faults is consistent with the high stacking fault energy of $\sim 1300 \text{ mJ/m}^2$ of the NbMoTaW system compared to the much smaller value for $\text{Al}_{0.1}\text{CoCrFeNi}$ ⁴¹. While the DXA is fairly reliable in determining defects in fcc systems, it is too simplistic for a bcc system where it may not detect defects such as planar faults and uncommon dislocations beyond screw and edge dislocations. Thus, the bcc defect analysis (BDA) tool is used to investigate common defects following the common neighbor analysis method utilized in OVITO^{30,42}. With the BDA tool we detect very small twin boundaries in the nodes of the nanoporous system that were not accounted for in the initial DXA sweep. The BDA also displayed a higher number of dislocations compared to the DXA tool, especially in the fracturing ligament. For initial strain values before 14%, no defects were identified in the ligaments. Increasing strains displayed the nucleation of twin boundaries with dislocations surrounding the edges was observed (Fig. 6a). The tool does not determine the dislocation types, but other common bcc systems display a $1/6\langle 111 \rangle$ partial dislocation as the most probable type of dislocation that is generally responsible for the twinning mechanism which is the primary deformation mechanism in bcc Fe nanopillars⁴³. The twinning partial dislocations allow the twin boundaries at both ends of the ligament to slip toward the center (Fig. 6b), where they interact to form a complex dislocation bundle (Fig. 6c). This dislocation bundle appears to be the main catalyst for atom removal from the notch of the ligament leading to fracturing (Fig. 6d).

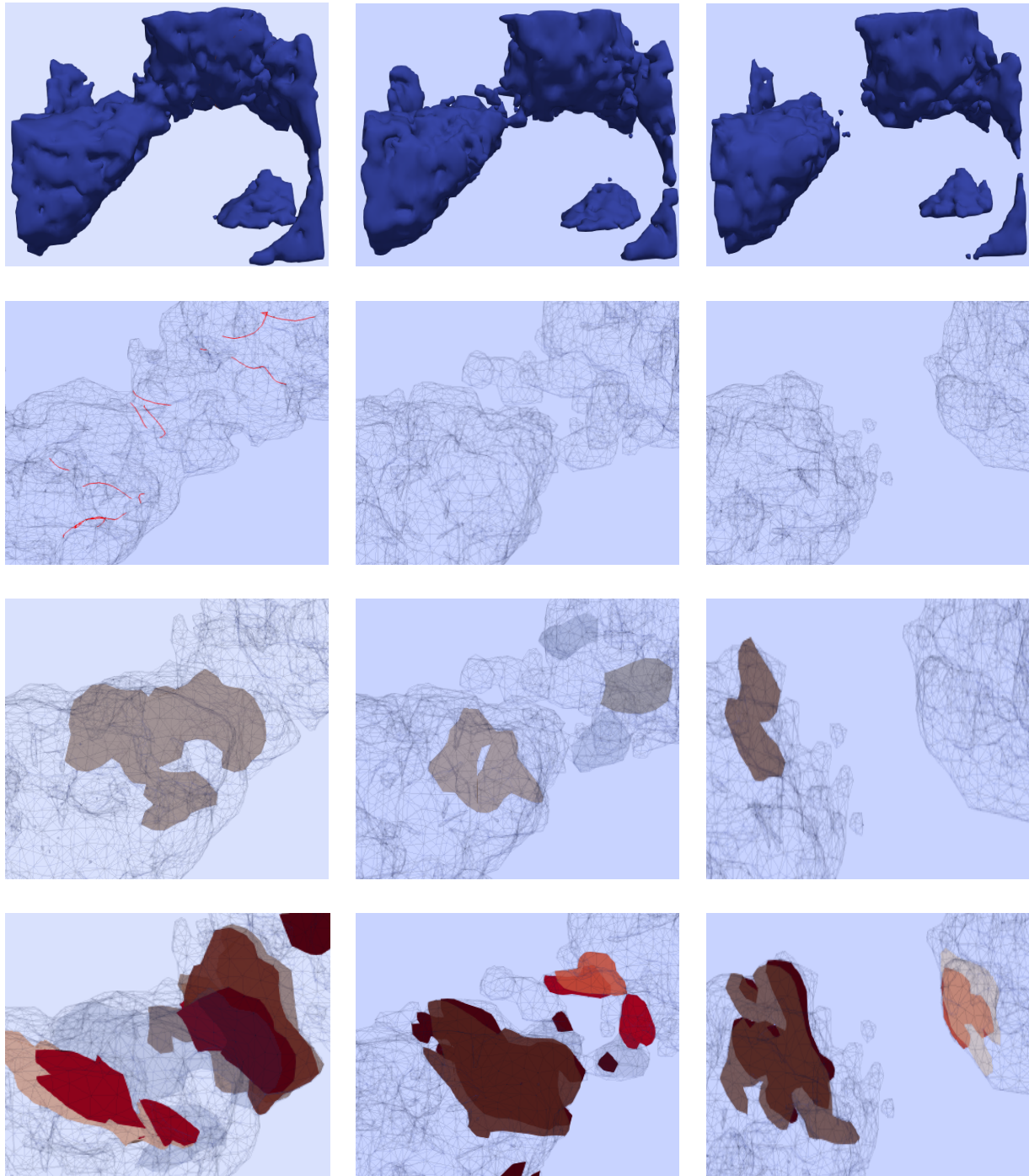


Figure 5. The fracture process of the 28.9% relative density 4.23 nm ligament size nanoporous $\text{Al}_{0.1}\text{CoCrFeNi}$ HEA under tensile testing. This shows (first row) the surface solid mesh outlining the atomic surface, (second row) dislocations colored red in the ligament, (third row) twin boundaries, and (fourth row) stacking faults. The strain values represented are 22.5%, 26.25%, and 31.25%, respectively (color in print).

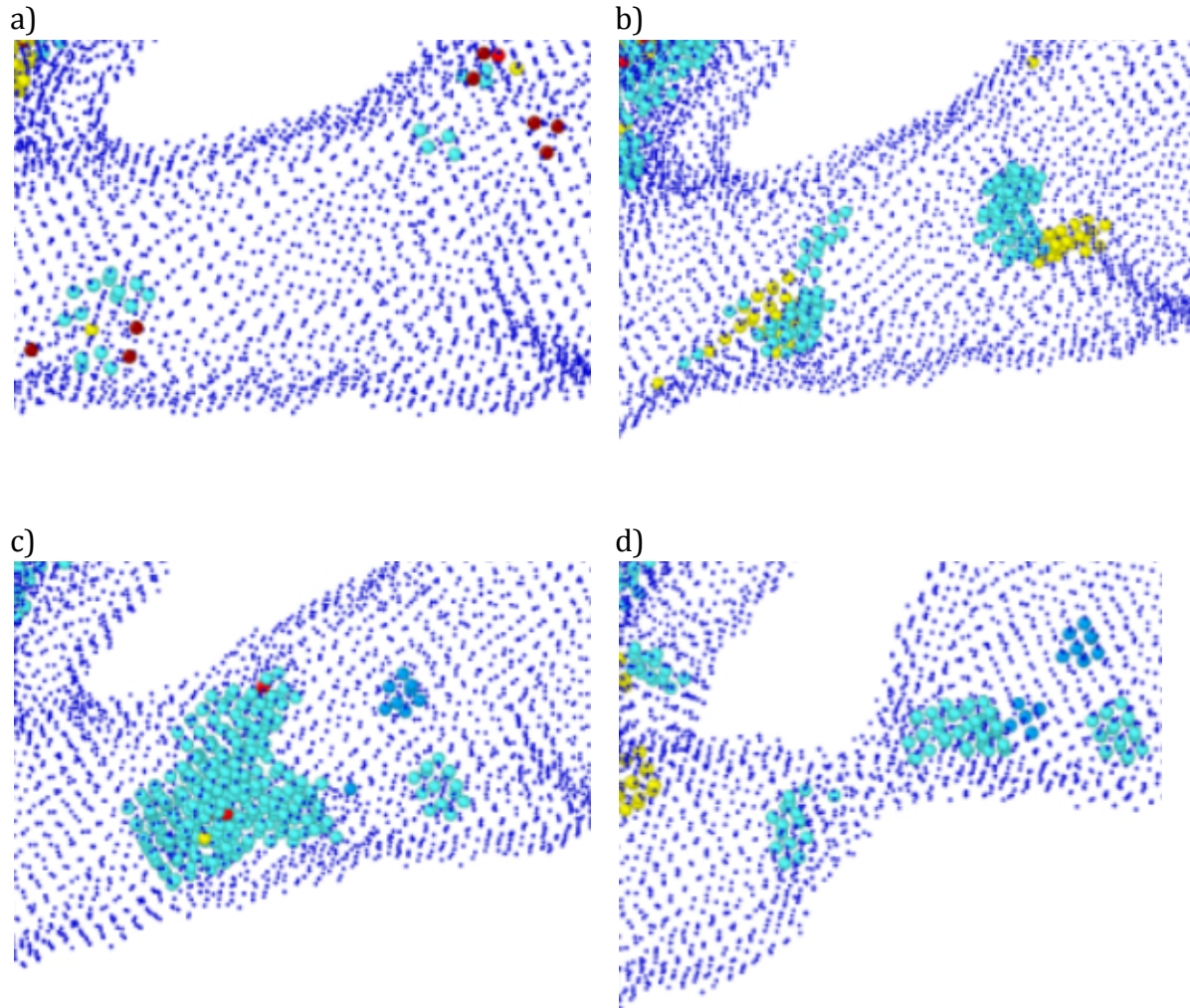


Figure 6. The fracture process of the 28.0% relative density 4.79 nm ligament size nanoporous NbMoTaW under tensile testing. The dark blue spheres are surface atoms, light blue are vacancies, green are atoms outlining dislocations, yellow are twin boundary atoms, and red are unidentifiable atoms. The strain values are 14% (a), 15% (b), 18% (c), and 20% (d).

2.4 Defect Analysis in Nanoporous Systems

Fig.6 shows the concentrations of dislocations and stacking faults at 600 and 1273 K for the $\text{Al}_{0.1}\text{CoCrFeNi}$ system as a function of strain for both tension and compression tests. For both test geometries, an increase in temperature lowers the defect density as higher temperatures facilitate dislocation annihilation and increase the stacking fault energy^{44,45}. For both temperatures, the dislocation and stacking fault densities are lower for lower relative density nanoporous $\text{Al}_{0.1}\text{CoCrFeNi}$ samples. This trend can be explained by the

higher surface area to volume ratio of the lower relative density systems that facilitates defect annihilation¹⁷. The higher dislocation density for smaller ligament sizes at lower temperatures can be attributed to more defect pileups in the joints (In Supplementary Materials SFig. 4) of the nanoporous system where the smaller ligament systems have more junctions²⁹. For higher temperatures, however, the defect concentration becomes lower in smaller ligaments as faster defect migration and annihilation starts to dominate over defect pileup^{17,46}.

In general, the dislocation density seems to be less sensitive than the stacking fault density towards changes in temperatures or test geometry. For both test geometries, the dislocation density of nanoporous $\text{Al}_{0.1}\text{CoCrFeNi}$ (Fig. 7a,b and Fig. 8a,b) displays a sharp increase for increasing strains up to 10%. For higher strains, the dislocation density plateaus in tensile testing whereas it continually increases in compression tests. The stacking fault density generally increases more steadily and for nanoporous systems is heavily dependent on temperature and testing type (Fig. 7c,d and Fig. 8c,d). Under compression at high temperatures, the defect concentration increases up to approximately 55% strain after which it slowly decreases with most of the curves remaining below the nanocrystalline system. At lower temperatures, the stacking fault density increases throughout the compression with many nanoporous systems showing concentrations above the nanocrystalline systems. Under tensile testing, the stacking fault densities appear to follow more closely the dislocation concentration trends with a stronger increase up to 10% strain followed by a more gradual increase for higher strains with most of the ligament systems staying beneath the nanocrystalline systems concentration for both temperatures. Dislocations appear to correlate with trends in the stress strain curves (Fig. 3). Under compression when analyzing similar density systems, the deviation of dislocation densities corresponds with the intersection of stresses. For the 1273 K compression system, the 47.8% and 46.9% relative densities remain at similar defect densities up to 45% strain when the 46.9% density system has a sharper reduction in dislocation density. This is approximately the strain value where the 46.9% density system crosses and surpasses stress values of the 47.8% system. The dislocation densities also suggest that for similar relative density systems, lower dislocation densities represent higher stresses under compression and higher dislocation densities represent higher stresses under tension. A similar phenomenon is seen where higher stacking fault densities appear to correlate with higher stresses. This can be seen where the 65.9% relative density shows a larger decrease in stacking fault density with increasing temperature compared to the 67.2% relative density system and shows a higher decrease in ultimate stress.

By contrast, no stacking fault defects were observed for any of the NbMoTaW nanoporous systems. While metastable stacking faults in bcc crystal structures are crucial for dissociation of partial dislocations, the absence of stacking faults can be attributed to the high stacking fault energy of bcc crystal structures^{41,47}. The dislocation density is lower under the tensile deformation compared to compression (Fig. S5). This could be caused by a tension-compression dislocation glide velocity asymmetry where tensile deformation could lead to a higher dislocation velocity where the dislocations would interact and annihilate at the surface of the ligaments^{17,48}. Another explanation comes from elongation of ligaments that increases the surface-to-volume ratio increasing the dislocation annihilation rate. Temperature has a far less pronounced effect on the dislocation density compared to $\text{Al}_{0.1}\text{CoCrFeNi}$. The nanoporous NbMoTaW systems have virtually no change in

dislocation density with different temperatures for tensile deformation whereas there is a small change under compression with higher dislocation densities for higher temperatures. While dislocation velocity increases with higher temperature, the dislocation formation also increases. Depending on the HEA, dislocation velocity will be heavily impeded, especially for bcc materials due to slow screw dislocation motion and sluggish diffusion of defects in HEAs ⁴⁹. For compression, the formation of dislocation increases more than the dislocation velocity and annihilation for higher temperatures.

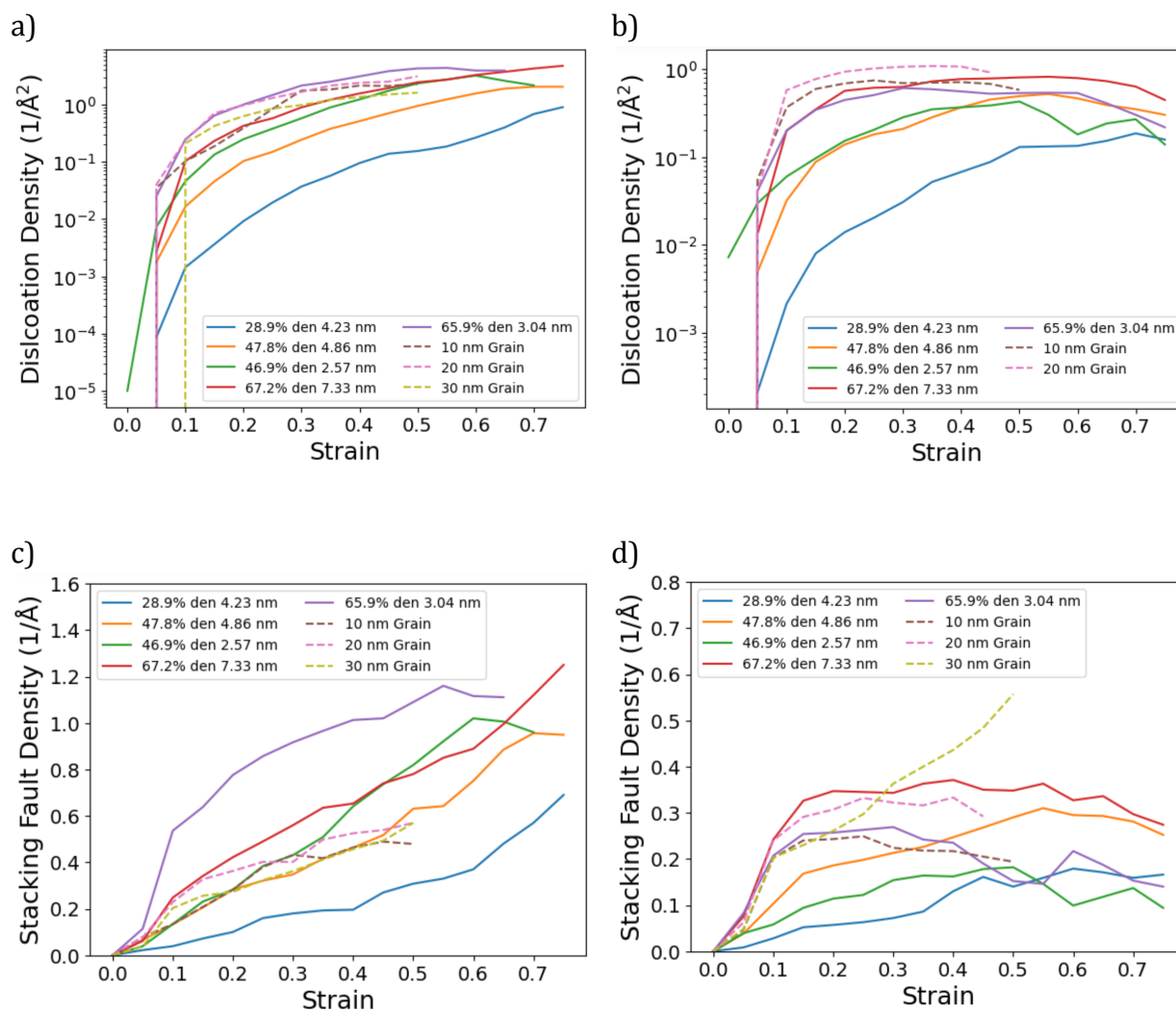


Figure 7. Stacking fault and dislocation concentration vs. strain curves for the $\text{Al}_{0.1}\text{CoCrFeNi}$ HEA systems under compression at 600 K (left column) / 1273 K (right column). NC represents nanocrystalline systems (color in print).

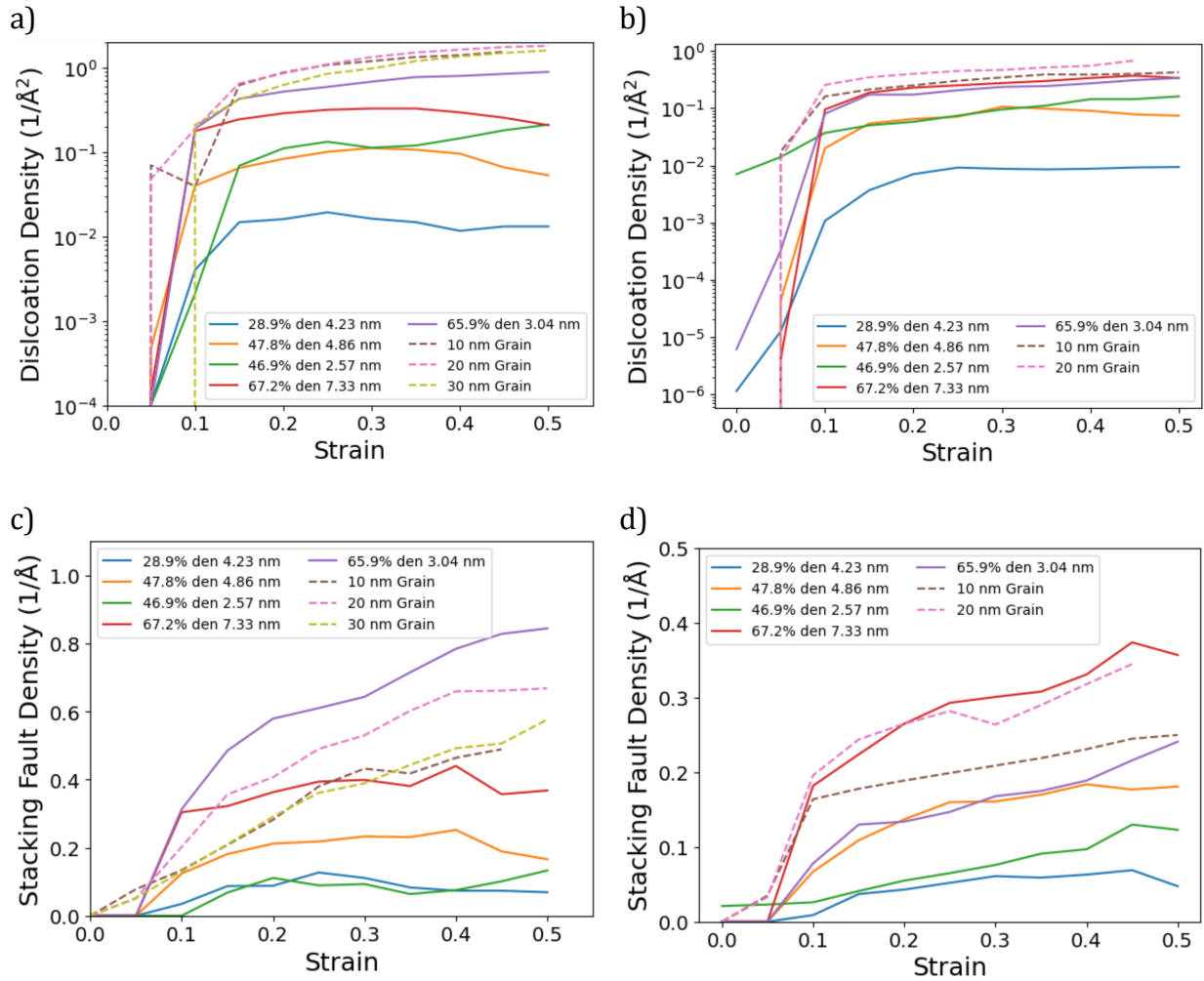


Figure 8. Stacking fault and dislocation concentration vs. strain curves for the Al_{0.1}CoCrFeNi HEA systems under tension at 600 K (left column) / 1273 K (right column). NC represents nanocrystalline systems (color in print).

Burgers vector analysis of the Al_{0.1}CoCrFeNi system reveals that Shockley partials with burgers vector $a/6\langle 112 \rangle$ dominate at low strain for both high and low temperature experiments. While this dislocation type remains the most common, other dislocation types including $a/3\langle 100 \rangle$ stair rod dislocations and $a/3\langle 110 \rangle$ Lomer dislocations are observed. These dislocation types are quite common in experimental analysis of bulk Al_{0.1}CoCrFeNi^{26,38}. Noticeable changes in dislocation types appear with further increasing strain: ligament systems with strain values of about 35% and higher begin to produce dislocation types with Burgers vectors $a/18\langle 721 \rangle$ and $a/18\langle 552 \rangle$ which appears to be associated with grain boundaries in the fcc lattice structure⁵⁰. As the strain further increases, this dislocation type begins to overtake the Shockley partial. The sudden change in dislocation types can be attributed to grain boundary formation as ligaments start to contact each other under high

compressive strain (Fig. 9). The strain value where these dislocation types appear is dependent on the relative density of $\text{Al}_{0.1}\text{CoCrFeNi}$ nanoporous system test, with lower strain values for higher relative density samples. Smaller ligament systems appear to play a role in dislocation development by increasing the strain value by 10% that would allow for the appearance of the $a/18\langle 721 \rangle$ and $a/18\langle 552 \rangle$ burgers vector dislocations when considering similar relative densities. This is analogous to findings of grain boundary formation during thermal coarsening in nanoporous Au⁵¹. As for the NbMoTaW system, the most common dislocation type during both tension and compression is the $a/2\langle 111 \rangle$ edge and screw dislocations. When compared to other MD and Density Functional Theory calculations, edge dislocations are found to be important in controlling the strength in refractory HEAs^{41,52}. At higher strain values, $a/2\langle 111 \rangle$ dislocations remain as the most prominent dislocations, but other less common dislocations like $a\langle 100 \rangle$ and $a\langle 110 \rangle$ also increase in density as strain values increase. The particular dislocation of $a\langle 110 \rangle$ is another dislocation type that is also seen in NbMoTaW for strength control⁵².

An additional investigation into $\text{Al}_{0.1}\text{CoCrFeNi}$ nanopillars was conducted to investigate the dislocation/stacking fault interaction during compression and tensile tests. The simulations use a 7 nm size nanopillar under compression and tensile tests in the long directions following the same parameters of relaxation and compression as the bicontinuous structures (Fig. S6). The simulation shows the nanopillar surface outlined by the blue mesh, the deformation-induced stacking faults/twin boundaries being represented by the planes, and dislocations are displayed by lines. The stacking faults are prevalent in both compression and tensile tests, with few dislocations and more stacking faults in compressive tests similar to the observations in the bicontinuous nanoporous structures. The only observable dislocations were confined to the borders of the stacking faults and are identified as Shockley partial dislocations. This can especially be seen in the 19% strain under compressive conditions in Fig. S6 where one of the larger stacking faults broke apart and displayed dislocations outlining the border. The dislocations for the given systems are then confined by the stacking faults that act as barriers to dislocation motion. No other dislocation types were observed in the simulations. This suggests that stacking faults behave as activation barriers for dislocation nucleation and motion, with many stacking faults being present due to the low stacking fault energy, behaving as multiple activation events for dislocation motion.

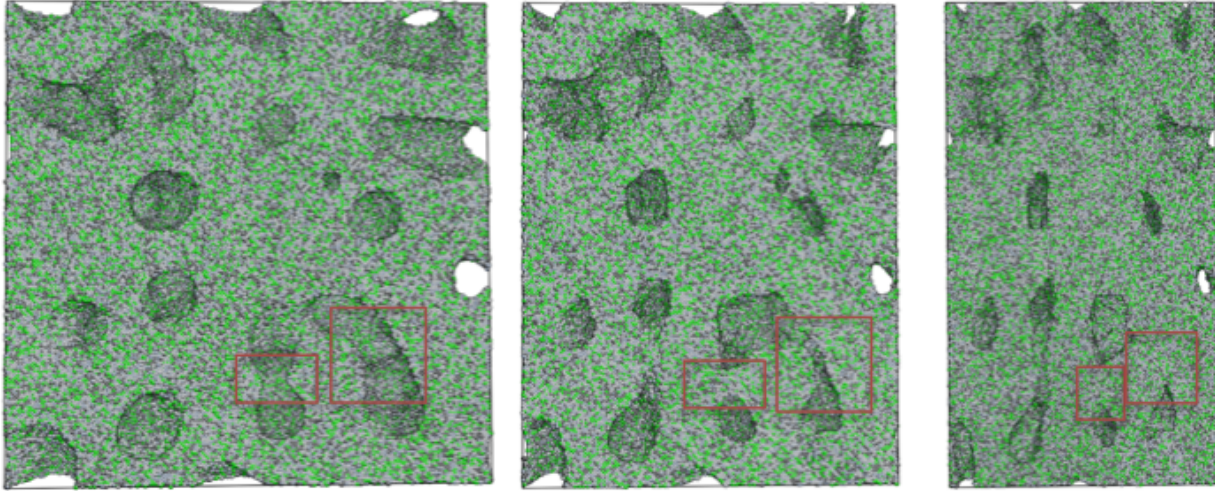


Figure 9. Simulation boxes showing the 67.2% relative density 7.33 nm $\text{Al}_{0.1}\text{CoCrFeNi}$ nanoporous system under compression at 298 K. The red boxes show the locations of pore sites being reduced and ligaments connecting with strains of 0/25/50% (color in print).

2.5 Surface Energy Analysis

The surface energy (table 5) of the nanoporous $\text{Al}_{0.1}\text{CoCrFeNi}$ systems was calculated by first obtaining the total energy of the nanoporous $\text{Al}_{0.1}\text{CoCrFeNi}$, subtracting the total energy of the bulk that has the same number of atoms at given temperatures, and then dividing by the surface area. The surface areas of the nanoporous HEA systems (table 6) were calculated using OVITO software for calculating surface mesh with a probing radius of 4 ³⁰. Higher relative densities tended to have lower surface energy with smaller ligament sizes having twice the value of the larger ligaments, consistent with the larger number of surface atoms in smaller ligament systems ⁵³. One interesting phenomenon is that surface energy tends to increase with increasing temperature for all relative densities. This is typically not the case for bulk metals where surface energy decreases with increasing temperature ⁵⁴. Zhang et. al. determined that surface energy plays a role in increasing the strength of nanoporous materials ⁵⁵. Thus the high surface energies with increasing temperature (table 5) suggest hardening of the material after relaxation. This phenomenon can be partially explained by reduced coarsening of the ligaments in nanoporous $\text{Al}_{0.1}\text{CoCrFeNi}$ that would otherwise compromise the functional properties of nanoporous materials associated with their high surface energy by increasing ligament size ⁵⁶. It was found that nanoporous TiVNbMoTa and TaMoNbVNi had a lower than expected coarsening effect for increasing temperatures ^{56,57}. There are many other possible contributions to reduced coarsening for nanoporous $\text{Al}_{0.1}\text{CoCrFeNi}$ such as bulk diffusion, surface chemistry, and phase separation ⁵⁷. With a reduced coarsening, surface energy decrease is reduced with increasing temperature, however the increase in surface energy has not been observed and further study is needed to understand this ⁵⁷.

The surface energy also appears to change depending on the mechanical test that is conducted. Fig. 10 shows the surface energy under compressive and tensile tests for the 600 K and 1273 K systems. For tensile tests, the surface energies initially increase then stay stable for the majority of the strain with slight decrease at higher strains. Increasing temperature reduces these increases in surface energy with some systems losing surface energy at higher strains. Under compression, the surface energy of the systems appears to follow similar trends with an initial increase, followed by a plateau region, and a growth region at higher strains. The surface energy graphs under compression are similar to surface energy analysis in previous simulations conducted by Worden J. and Hin C. based on nanoporous W with similar trends in surface energy vs. strain curves. Temperature impacts the surface energy differently for compression compared to tensile tests where an increasing temperature negatively impacts the surface energy for tensile at higher strains but increases under compression at higher strains. MD analysis of Au nanowires found that decreasing surface energy leads to a change in from twinning to perfect dislocation plasticity⁵⁸. Analyzing the second highest surface energy system of 46.9% relative density with 3.04 nm ligaments did not show a change in the deformation mechanism. Higher surface energies would be needed to change the deformation mechanism. It is important to note the curve for the 46.9% density, 2.57 nm ligament size system appears to behave differently at higher temperatures and higher strains compared to the other systems (Fig. 10). This can be seen in the tensile tests where the surface energy continuously increases for the 46.9% density, 2.57 nm ligament system whereas the other systems either plateau or decrease. This could potentially be due to the small ligament sizes breaking down similarly to the 27.8% density, 2.20 nm ligament system that was unstable at higher temperatures that could have been exacerbated by the high strains. Compression tests also display this where the 600 K temperature shows the 46.9% density system having lower surface energy at higher strains compared to the 65.9% relative density, 3.04 nm ligament size system. This changes when 1273 K is studied and the surface energy for 46.9% density sharply increases compared to the other curves of the system around 20% strain and has the highest value of surface energy for greater values of strain.

Table 5. Surface energy of nanoporous HEA systems with varying temperatures.

System	Surface Energy 298 K (mJ/m ²)	Surface Energy 600 K (mJ/m ²)	Surface Energy 900 K (mJ/m ²)	Surface Energy 1273 K (mJ/m ²)
28.9% den 4.23 nm	1213.49	1227.33	1249.40	1243.10
28.7% den 2.20 nm	2072.21	-	-	-
47.8% den 4.86 nm	1050.32	1072.66	1106.64	1126.49
46.9% den 2.57 nm	1601.33	1638.84	1657.15	1729.40
67.2% den 7.33 nm	643.80	757.91	805.61	851.42
65.9% den 3.04 nm	1350.66	1417.91	1465.06	1508.14

Table 6. Surface area of nanoporous HEA systems.

System	Surface Area (m ²)
28.9% den 4.23 nm	2.13797×10^{-14}
28.7% den 2.20 nm	4.22855×10^{-14}
47.8% den 4.86 nm	2.46707×10^{-14}
46.9% den 2.57 nm	5.80548×10^{-14}
67.2% den 7.33 nm	2.13217×10^{-14}
65.9% den 3.04 nm	5.19859×10^{-14}

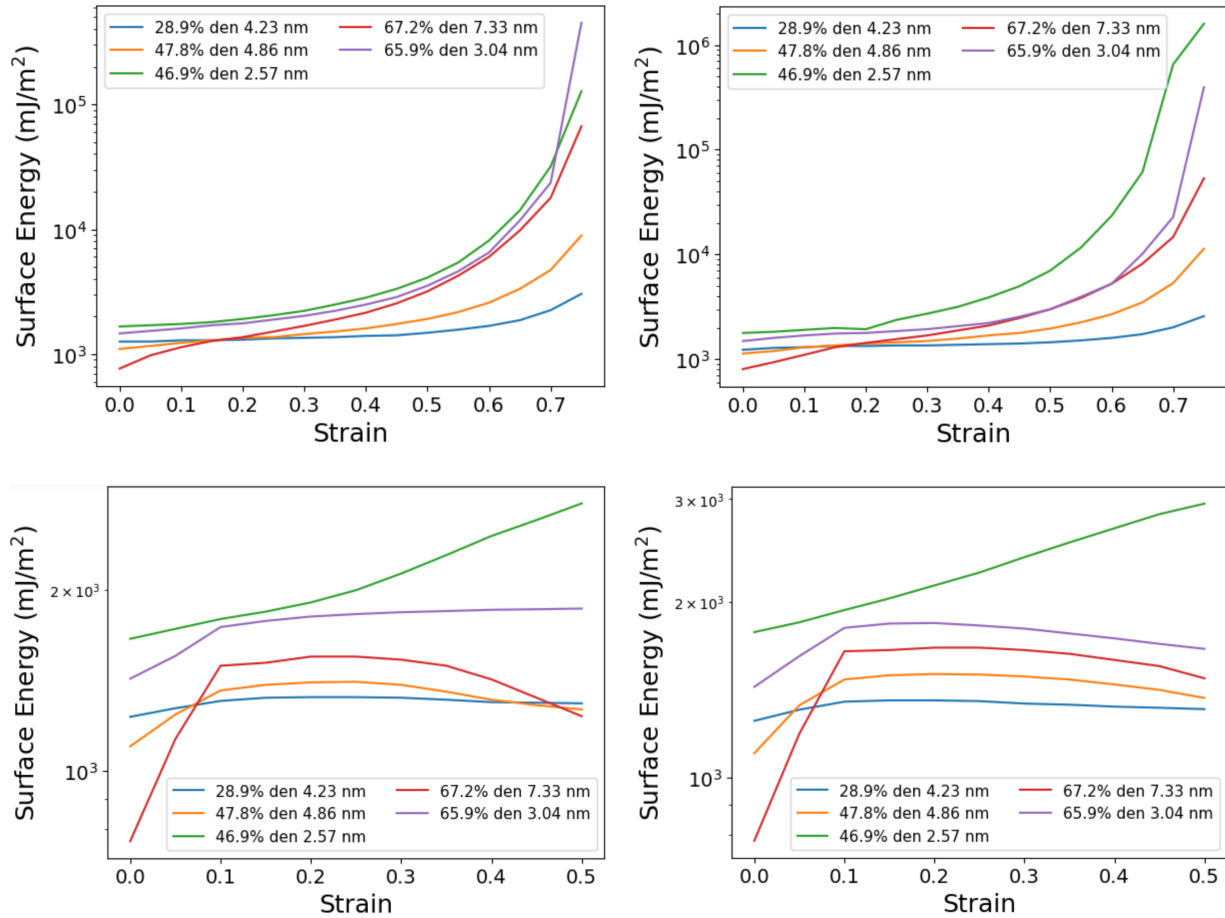


Figure 10. Surface energy as a change in strain for mechanical testing for compression (top row) and tension (bottom row) at 600 K (left column) / 1273 K (right column) (color in print).

Discussion

To highlight the remarkable mechanical properties of the nanoporous HEAs, the systems are compared to other nanoporous materials (Fig. S7). Most notably, their yield stress is much higher than that of other studied nanoporous systems with similar relative densities studied by both simulation and experimentals in compression or tension. Nanoporous W studied by MD simulations in prior research, conducted by Worden J. and Hin. C., shows the highest yield strengths of nanoporous materials along with nanoporous NbMoTaW. Further investigation between fcc and bcc nanoporous systems are discussed in Supplementary Discussion 4. While nanoporous W outcompetes nanoporous Al_{0.1}CoCrFeNi when considering yield stress, the two-times higher density of W compared to HEA brings

its specific strength below that of the nanoporous HEAs. The excellent performance of nanoporous HEA could be caused by a synergistic effect related to the high strength of HEAs through sluggish diffusion and the dislocation reduction of bicontinuous nanoporous structures^{49,59}. The dislocation starvation mechanism can be observed when comparing the lower dislocation densities between the nanoporous and nanocrystalline systems in Fig. 8. This mechanism is especially prominent in the lower relative densities that inherently have a lower number of nodes that demonstrate the highest defect density in nanoporous systems as can be observed in Fig. S4. The sluggish diffusion mechanism of HEAs can be observed in the comparison of dislocation densities with nanoporous single element W. An additional investigation analyzing the dislocation densities under compression at 600 K is displayed in Fig. S8. The W nanoporous structure is taken as the exact structure that is used for the NbMoTaW system but with different average ligament sizes due to the lattice constants. The dislocation densities are significantly higher in the HEA systems when comparing the similar nanoporous structures signifying a faster dislocation mobility in W due to the removal of these defects at the surface. A potential explanation is a lower activation energy for dislocation nucleation in the HEAs, but the 28.0% relative density W has dislocation densities at lower strain values compared to the HEA. This implies either an equal or lower activation energy for dislocation nucleation in W compared to NbMoTaW.

There appears to be an additional mechanism for the outstanding mechanical properties that come from the sluggish diffusion of dislocations in HEAs⁶⁰. In fcc crystal structures under deformation, Shockley partial dislocations are primarily formed by the splitting of a perfect dislocation $a/2(110)$ due to the very low stacking fault energy and high Peierls stress of unit dislocation motion⁶⁰. There are MD simulations of $Al_{0.1}CoCrFeNi$ with identifiable perfect dislocations under deformation, but these nucleate from prior GBs and quickly dissociate into partial dislocations with stacking faults³⁸. Analysis of the types of dislocations in the nanoporous and nanopillar systems showed the complete absence of perfect dislocations suggesting a very short lifetime of the perfect dislocation due to rapid splitting into partials. The primary deformation mechanism would appear to be slip of (111) stacking faults and the Shockley partial dislocations bounding the stacking faults in the $\langle 110 \rangle$ direction that is different to the perfect dislocation movement in the highest packed $\langle 111 \rangle$ direction⁶¹. This is different from nanoporous and nanopillar gold systems that display a mix of partial dislocations, perfect dislocations, and perfect dislocation loops together leading to higher deformation^{62,63}. These deformation mechanisms are included with other larger defects such as twins and stacking faults. The stacking fault and partial dislocation in $Al_{0.1}CoCrFeNi$ ligaments will move in the $\langle 110 \rangle$ direction until they come into contact with a surface, removing one of the partial dislocations that comes into contact with the surface, as observed in the nanoporous and nanopillar $Al_{0.1}CoCrFeNi$ systems where the stacking faults are bounded by the surface of the ligament and one dislocation. Once one of the partials is annihilated at the surface, the stacking fault is trapped in that position within the ligament due to the attractive forces between the second partial dislocation and the stacking fault. The stacking fault would not have as much of an issue diffusing in a ligament oriented in the $\langle 110 \rangle$ direction, but would still have trouble bounded by a small enough ligament size. Inhibiting partial dislocation mediated stacking fault slip provides strong work hardening⁶⁴. This gives rise to a potential link between ligament size and average stacking fault size for fcc nanoporous high entropy alloys. As is shown in tables 1 and 2, the ligaments investigated for nanoporous $Al_{0.1}CoCrFeNi$ are shown to have a higher yield

strength for the larger ligaments, even though the common thought is that smaller ligament sizes leads to higher strength⁶⁵. However, by going smaller than a critical ligament size, the strength decreases. Having ligaments of similar sizes as the stacking faults would increase the number of atoms and strength of the individual ligaments while maintaining the locked stacking fault mechanism where stacking faults will not leave the ligaments and create more trapping sites for defects⁶⁶. When analyzing the NbMoTaW system, the sluggish diffusion mechanism reduces dislocation motion such that the inherently difficult screw dislocation mobility and edge dislocation motion are much more comparable than in single element materials^{41,67}. The reason for minimal dislocation observation in the ligaments could be attributed to the preferential nucleation of dislocations on surfaces that are oriented in the $\langle 111 \rangle$ direction⁶⁸. This orientation is primarily found in the nodes of the nanoporous structure where ligaments connect whereas the orientation of the surface of the ligaments is typically $\langle 100 \rangle$ or $\langle 110 \rangle$. Combining the nucleation of dislocations in the nodes with similar dislocation speed for screw and edge dislocations increases the likelihood of a dislocation pileup in the center of the nodes, strengthening the material through dislocation forest hardening and reducing the probability of a dislocation deforming the ligaments⁶⁹.

Conclusions

The MD results discussed in this work demonstrates the exceptional mechanical properties of nanoporous High-Entropy Alloys (HEAs). The materials offer a remarkable combination of high strength, low Young's modulus, and low density, occupying a previously unoccupied region of the specific modulus-strength phase space. The molecular dynamics simulations suggest that the high strength of nanoporous HEAs is due to the dual mechanism of dislocation starvation and sluggish diffusion. The reduced dislocation motion impacts the defect evolution differently depending on whether the HEA is an fcc or bcc structure. For the fcc structure, the perfect edge dislocation is reduced due to the sluggish diffusion mechanism, making it more likely for stacking faults to form in the ligaments due to the low stacking fault energy. Stacking faults in the ligaments are then trapped due to the bounding of the stacking fault with the surface and are additionally limited due to the orientation of ligaments that hinders partial dislocation motion bounding stacking faults. For the bcc structure, the sluggish diffusion contributes to the dislocation pileup in the nodes of nanoporous structure, causing dislocation forest hardening. The similar mobility of screw and edge dislocations leads to the interaction of a large number of dislocations in the center of the nodes thus creating large pile ups and reducing the number of dislocations that would travel into ligaments to cause deformation. The lack of dislocation nucleation in the ligaments comes from the preferential (111) direction of the surfaces of the nanoporous structure, but is common in the nodes. Furthermore, the study observed that tailoring the ligament size and relative density of the material yields varying responses in defect density concentrations and surface energy. Lower relative densities were found to be associated with reduced defect densities and higher initial surface surfaces energies. Further analysis of these structures will provide valuable insights into the unique mechanisms at play in nanoporous HEAs.

Contributions:

B. J.: Writing-review and editing

H. C.: Supervision, Writing-review and editing

W. J.: Formal Analysis, Investigation, Software, Visualization, Writing-original draft, writing-review and editing.

Competing Interest:

The authors declare no competing interest.

Supplementary Information is available for this paper upon reasonable request.

Reference

1. Xie, L. *et al.* Molecular dynamics simulation of Al–Co–Cr–Cu–Fe–Ni high entropy alloy thin film growth. *Intermetallics* **68**, 78–86 (2016).
2. Biener, J., Hodge, A. M. & Hamza, A. V. Microscopic failure behavior of nanoporous gold. *Appl. Phys. Lett.* **87**, 121908 (2005).
3. Griffiths, E., Soyarslan, C., Bargmann, S. & Reddy, B. D. Insights into fracture mechanisms in nanoporous gold and polymer impregnated nanoporous gold. *Extreme Mech. Lett.* **39**, 100815 (2020).
4. Kim, Y.-C. *et al.* Indentation size effect in nanoporous gold. *Acta Mater.* **138**, 52–60 (2017).
5. Stuckner, J. Investigating the Origin of Localized Plastic Deformation in Nanoporous Gold by in Situ Electron Microscopy and Automatic Structure Quantification. (Virginia Polytechnic Institute and State University, 2019).
6. Zhang, Y. *et al.* Characterization of the deformation behaviors under uniaxial stress for bicontinuous nanoporous amorphous alloys. *Phys. Chem. Chem. Phys.* **24**, 1099–1112 (2022).
7. Eleti, R. R., Klimova, M., Tikhonovsky, M., Stepanov, N. & Zhrebttsov, S. Exceptionally high strain-hardening and ductility due to transformation induced plasticity effect in Ti-rich high-entropy alloys. *Sci. Rep.* **10**, 13293 (2020).
8. Li, G. *et al.* Simultaneously enhanced strength and strain hardening capacity in FeMnCoCr high-entropy alloy via harmonic structure design. *Scr. Mater.* **191**, 196–201 (2021).
9. Wang, X., Guo, W. & Fu, Y. High-entropy alloys: emerging materials for advanced functional applications. *J. Mater. Chem. A* **9**, 663–701 (2021).
10. Li, Z., Zhao, S., Ritchie, R. O. & Meyers, M. A. Mechanical properties of high-entropy alloys with emphasis on face-centered cubic alloys. *Prog. Mater. Sci.* **102**, 296–345 (2019).
11. Dong, W. *et al.* Applications of High-Pressure Technology for High-Entropy Alloys: A Review. *Metals* **9**, 867 (2019).
12. Fentahun, M. & Savas, M. Materials Used in Automotive Manufacture and Material Selection Using Ashby Charts. *Int. J. Mater. Eng.* **8**, (2018).
13. Inagaki, I., Takechi, T., Shirai, Y. & Ariyasu, N. Application and Features of Titanium for the Aerospace Industry. *Nippon Steel Sumitomo Met. Tech. Rep.* (2014).
14. Surani, F. B., Kong, X., Panchal, D. B. & Qiao, Y. Energy absorption of a nanoporous

- system subjected to dynamic loadings. *Appl. Phys. Lett.* **87**, 163111 (2005).
15. El-Atwani, O. *et al.* Outstanding radiation resistance of tungsten-based high-entropy alloys. *Sci. Adv.* **5**, eaav2002 (2019).
 16. Xia, S. Q., Yang, X., Yang, T. F., Liu, S. & Zhang, Y. Irradiation Resistance in Al_xCoCrFeNi High Entropy Alloys. *JOM* **67**, 2340–2344 (2015).
 17. Beyerlein, I. J. *et al.* Radiation damage tolerant nanomaterials. *Mater. Today* **16**, 443–449 (2013).
 18. Guo, Y. *et al.* Study on the microstructural evolution in NbMoTaW series refractory multi-principal element alloy films by low-energy and high-flux He ions irradiation. *Surf. Coat. Technol.* **452**, 129140 (2023).
 19. Gibson, L. J. & Ashby, M. F. *Cellular solids: structure and properties*. (CUP, 1999).
 20. Joseph, J., Stanford, N., Hodgson, P. & Fabijanic, D. M. Tension/compression asymmetry in additive manufactured face centered cubic high entropy alloy. *Scr. Mater.* **129**, 30–34 (2017).
 21. Giallonardo, J. D., Erb, U., Aust, K. T. & Palumbo, G. The influence of grain size and texture on the Young's modulus of nanocrystalline nickel and nickel–iron alloys. *Philos. Mag.* **91**, 4594–4605 (2011).
 22. Pia, G. & Delogu, F. Mechanical Properties of Nanoporous Au: From Empirical Evidence to Phenomenological Modeling. *Metals* **5**, 1665–1694 (2015).
 23. Qian, L. H., Yan, X. Q., Fujita, T., Inoue, A. & Chen, M. W. Surface enhanced Raman scattering of nanoporous gold: Smaller pore sizes stronger enhancements. *Appl. Phys. Lett.* **90**, 153120 (2007).
 24. Mohammed, A. A., Haris, S. M. & Al Azzawi, W. Estimation of the ultimate tensile strength and yield strength for the pure metals and alloys by using the acoustic wave properties. *Sci. Rep.* **10**, 12676 (2020).
 25. Alagarsamy, K. *et al.* Mechanical Properties of High Entropy Alloy Al_{0.1}CoCrFeNi for Peripheral Vascular Stent Application. *Cardiovasc. Eng. Technol.* **7**, 448–454 (2016).
 26. Liu, C., Yang, Y. & Xia, Z. Deformation mechanism in Al_{0.1}CoCrFeNi Σ 3(111)[110] high entropy alloys – molecular dynamics simulations. *RSC Adv.* **10**, 27688–27696 (2020).
 27. Hu, Y. L. *et al.* First-principle calculation investigation of NbMoTaW based refractory high entropy alloys. *J. Alloys Compd.* **827**, 153963 (2020).
 28. Clark, P. Computation Aided Design Of Multicomponent Refractory Alloys With A Focus On Mechanical Properties. (University of Mississippi, 2016).
 29. Giri, A., Tao, J., Wang, L., Kirca, M. & To, A. C. Compressive Behavior and Deformation Mechanism of Nanoporous Open-Cell Foam with Ultrathin Ligaments. *J. Nanomechanics Micromechanics* **4**, A4013012 (2014).
 30. Stukowski, A. Visualization and analysis of atomistic simulation data with OVITO–the Open Visualization Tool. *Model. Simul. Mater. Sci. Eng.* **18**, 015012 (2010).
 31. Ahrens, J., Geveci, B. & Law, C. ParaView: An End-User Tool for Large-Data Visualization. in *Visualization Handbook* 717–731 (Elsevier, 2005). doi:10.1016/B978-012387582-2/50038-1.
 32. Sokkalingam, R. *et al.* Powder metallurgy of Al_{0.1}CoCrFeNi high-entropy alloy. *J. Mater. Res.* **35**, 2835–2847 (2020).
 33. Yang, Y.-C., Liu, C., Lin, C.-Y. & Xia, Z. Core effect of local atomic configuration and design principles in Al_xCoCrFeNi high-entropy alloys. *Scr. Mater.* **178**, 181–186 (2020).
 34. Li, J. *et al.* Microstructure-sensitive mechanical properties of nanoporous gold: a

- molecular dynamics study. *Model. Simul. Mater. Sci. Eng.* **26**, 075003 (2018).
35. Beets, N., Stuckner, J., Murayama, M. & Farkas, D. Fracture in nanoporous gold: An integrated computational and experimental study. *Acta Mater.* **185**, 257–270 (2020).
 36. Granberg, F. *et al.* Mechanism of Radiation Damage Reduction in Equiatomic Multicomponent Single Phase Alloys. *Phys. Rev. Lett.* **116**, 135504 (2016).
 37. Shih, M., Miao, J., Mills, M. & Ghazisaeidi, M. Stacking fault energy in concentrated alloys. *Nat. Commun.* **12**, 3590 (2021).
 38. Sharma, A. & Balasubramanian, G. Dislocation dynamics in Al_{0.1}CoCrFeNi high-entropy alloy under tensile loading. *Intermetallics* **91**, 31–34 (2017).
 39. Liu, F. X., Cocks, A. C. F. & Tarleton, E. Dislocation dynamics modelling of the creep behaviour of particle-strengthened materials. *Proc. R. Soc. Math. Phys. Eng. Sci.* **477**, 20210083 (2021).
 40. An, X., Ni, S., Song, M. & Liao, X. Deformation Twinning and Detwinning in Face-Centered Cubic Metallic Materials. *Adv. Eng. Mater.* **22**, 1900479 (2020).
 41. Li, X.-G., Chen, C., Zheng, H., Zuo, Y. & Ong, S. P. Complex strengthening mechanisms in the NbMoTaW multi-principal element alloy. *Npj Comput. Mater.* **6**, 70 (2020).
 42. Möller, J. J. & Bitzek, E. BDA: A novel method for identifying defects in body-centered cubic crystals. *MethodsX* **3**, 279–288 (2016).
 43. Sainath, G. & Choudhary, B. K. Deformation behaviour of body centered cubic iron nanopillars containing coherent twin boundaries. *Philos. Mag.* **96**, 3502–3523 (2016).
 44. Joardar *, J., Fillit, R. Y. & Fraczkiewicz, A. A study of thermal vacancies and dislocation structure in Fe–40 at.% Al. *Philos. Mag. Lett.* **85**, 299–309 (2005).
 45. Molnár, D. *et al.* Effect of temperature on the stacking fault energy and deformation behaviour in 316L austenitic stainless steel. *Mater. Sci. Eng. A* **759**, 490–497 (2019).
 46. Fan, Z. *et al.* Temperature-dependent defect accumulation and evolution in Ni-irradiated NiFe concentrated solid-solution alloy. *J. Nucl. Mater.* **519**, 1–9 (2019).
 47. Po, G. *et al.* A phenomenological dislocation mobility law for bcc metals. *Acta Mater.* **119**, 123–135 (2016).
 48. Gröger, R., Racherla, V., Bassani, J. L. & Vitek, V. Multiscale modeling of plastic deformation of molybdenum and tungsten: II. Yield criterion for single crystals based on atomistic studies of glide of $1/2\langle 111 \rangle$ screw dislocations. *Acta Mater.* **56**, 5412–5425 (2008).
 49. Chen, J. *et al.* A review on fundamental of high entropy alloys with promising high-temperature properties. *J. Alloys Compd.* **760**, 15–30 (2018).
 50. Van Tendeloo, G. Electron microscopy of interfaces in metals and alloys. By C. T. Forwood and L. M. Clarebrough, Adam Hilger, Bristol 1991, VI, 424 pp., hardcover, £ 75.00, ISBN 0-7503-0116-3. *Adv. Mater.* **4**, 692–693 (1992).
 51. Elder, K. L. M. *et al.* Grain boundary formation through particle detachment during coarsening of nanoporous metals. *Proc. Natl. Acad. Sci.* **118**, e2104132118 (2021).
 52. Yang, D., Chen, B., Li, S., Ding, X. & Sun, J. Effect of local lattice distortion on the core structure of edge dislocation in NbMoTaW multi-principal element alloys and the subsystems. *Mater. Sci. Eng. A* **855**, 143869 (2022).
 53. Vollath, D., Fischer, F. D. & Holec, D. Surface energy of nanoparticles – influence of particle size and structure. *Beilstein J. Nanotechnol.* **9**, 2265–2276 (2018).
 54. Zhang, X. *et al.* Temperature and size dependent surface energy of metallic nano-materials. *J. Appl. Phys.* **125**, 185105 (2019).

55. Zhang, W. X. & Wang, T. J. Effect of surface energy on the yield strength of nanoporous materials. *Appl. Phys. Lett.* **90**, 063104 (2007).
56. Okulov, A. V., Joo, S.-H., Kim, H. S., Kato, H. & Okulov, I. V. Nanoporous High-Entropy Alloy by Liquid Metal Dealloying. *Metals* **10**, 1396 (2020).
57. Joo, S. *et al.* Beating Thermal Coarsening in Nanoporous Materials via High-Entropy Design. *Adv. Mater.* **32**, 1906160 (2020).
58. Hwang, B. *et al.* Effect of surface energy on size-dependent deformation twinning of defect-free Au nanowires. *Nanoscale* **7**, 15657–15664 (2015).
59. Basu, I., Ocelík, V. & Hosson, J. T. M. D. Size effects on plasticity in high-entropy alloys. *J. Mater. Res.* **33**, 3055–3076 (2018).
60. Pasianot, R. & Farkas, D. Atomistic modeling of dislocations in a random quinary high-entropy alloy. *Comput. Mater. Sci.* **173**, 109366 (2020).
61. Korner, A. & Karnthalerauthor, H. P. Analysis of the stacking faults of dissociated glide dislocations in F.C.C. metals. *Phys. Status Solidi A* **68**, 19–28 (1981).
62. Dou, R. & Derby, B. Deformation mechanisms in gold nanowires and nanoporous gold. *Philos. Mag.* **91**, 1070–1083 (2011).
63. Melis, C. *et al.* Stiffening of nanoporous gold: experiment, simulation and theory. *Eur. Phys. J. Plus* **137**, 858 (2022).
64. Su, R. *et al.* The influence of stacking faults on mechanical behavior of advanced materials. *Mater. Sci. Eng. A* **803**, 140696 (2021).
65. Biener, J. *et al.* Size Effects on the Mechanical Behavior of Nanoporous Au. *Nano Lett.* **6**, 2379–2382 (2006).
66. Hsieh, K.-T. *et al.* Atomistic simulations of the face-centered-cubic-to-hexagonal-close-packed phase transformation in the equiatomic CoCrFeMnNi high entropy alloy under high compression. *Comput. Mater. Sci.* **184**, 109864 (2020).
67. Cao, T. *et al.* Strain rate dependent deformation behavior of BCC-structured Ti₂₉Zr₂₄Nb₂₃Hf₂₄ high entropy alloy at elevated temperatures. *J. Alloys Compd.* **891**, 161859 (2022).
68. Ruestes, C. J. *et al.* Plastic deformation of a porous bcc metal containing nanometer sized voids. *Comput. Mater. Sci.* **88**, 92–102 (2014).
69. Santos-Güemes, R. & LLorca, J. Dislocation dynamics analysis of the strengthening induced by shearable and non-shearable precipitates in the presence of dislocation pile-ups. *Eur. J. Mech. - ASolids* 105042 (2023)
doi:10.1016/j.euromechsol.2023.105042.

A New Class of Materials Based on Nanoporous High Entropy Alloys with Outstanding Properties: Supplementary Materials

Methods

The MD simulations were carried out using the open-source code LAMMPS using a three-dimensional cell with periodic boundary conditions with lengths of 44.625 nm x 44.625 nm x 44.625 nm¹. The bulk cell was produced by populating the cell with 7812500 fcc (3906250 bcc) structure atoms and randomly assigning the appropriate concentrations of Al, Co, Cr, Fe, and Ni (Nb, Mo, Ta, W) using AtomsK². The polycrystalline systems were produced using Voronoi Tessellation on the bulk cell with random grain orientations. Three different polycrystalline structures with 10/20/30 nm grain sizes were made. The method for producing nanoporous HEA followed similar methods used in producing bicontinuous nanoporous Au through dealloying simulation methods³. The demixing was conducted for 30/50/70% relative density of Ni using the fcc Ni-Cu system using a lattice parameter of 0.356 nm and an embedded atom method (EAM) interatomic potential for Ni-Cu^{4,5}. In addition, a fully repulsive Lennard-Jones potential is included and used as an addition to model the atomic interactions specifically between Ni and Cu to make the system fully immiscible³. A Nose/Hoover thermostat ensemble was used at a temperature above the melting point of the Ni-Cu system for a set amount of time to separate phases. Longer demixing times result in larger ligament sizes compared to shorter times where a demixing time of 100 ps is used for the larger ligaments and the smaller ligament systems were made with a total demixing time of 50 ps. After the set amount of time, the Cu phase is deleted and the remaining Ni phase is used as a skeleton for populating randomly placed atoms consisting of the Al_{0.1}CoCrFeNi disordered fcc crystalline phase. A similar setup was used following a W-Ta binary system using a lattice parameter of 0.316 nm to produce the nanoporous NbMoTaW system⁶. While this method does not represent a physically meaningful method of producing nanoporous materials in an experimental setting, it is sufficient in creating the bicontinuous structure for simulation analysis. A separate EAM potential is used to model the atomic interactions between the atoms in the nanoporous Al_{0.1}CoCrFeNi that have been used to model nanoindentation tests and plastic deformation⁷⁻⁹ and a MEAM potential is used to model NbMoTaW that reproduces elastic constants¹⁰. Defects in the system were analyzed using the Dislocation Analysis Tool for analyzing dislocation densities, dislocation types, and Stacking Fault/Twin Boundary formation¹¹. The average ligament diameter was calculated with a homemade procedure where atom locations would be selected to be the center of an expanding sphere. The sphere expands with a radial increase of half the lattice parameter and the surface of the sphere detects the local atom configuration to determine if a section of the sphere is in contact with the surface of the ligament. When the ligament surface is detected, the opposite side of the sphere is checked to see if it is also in contact with a surface. If it is, the distance is calculated as the diameter for a section of the ligament that will be averaged with the other diameters calculated for the system.

Supplementary Discussion 1:

In order to understand the impact of these materials on wider industries, nanoporous HEA is compared with Steel DP600, a primary component in car manufacturing¹². When considering the 28.9% relative density, 4.23 nm ligament size system, the density is found to be 2100.45 kg/m³ with specific strength and specific modulus of 0.159 MPa/(kg/m³) and 0.00769 GPa/(kg/m³), respectively. Steel DP600 has a density of 7800 kg/m³ with specific strength and specific modulus of 0.046 MPa/(kg/m³) and 0.0273 GPa/(kg/m³), respectively. Not only is the specific strength and modulus of the nanoporous HEA preferable for safety concerns, the density of nanoporous HEA is 26.9% the density of DP600 which would lead to lower fuel consumption and lower CO₂ emissions. It has been studied that, generally, a reduction of 100 kg leads to a reduction in CO₂ emissions of 11 g/km¹³. Steels generally make up around 70% of a car's weight¹³, leading to an average weight in steel of 1319.59 kg given the average car weight of 1885.13 kg^{13,14}. Replacing steel with nanoporous HEA would lead to a weight reduction of 964.24 kg, reducing the vehicle weight to 49% of the original weight. This leads to a reduction in carbon emissions of 106.07 g/km and a savings in fuel consumption of 3.86 L per 100 km that is a reduction of 40% fuel use. Nanoporous HEA appears to be an all-round better option compared to conventional steels for car manufacturing for fuel reduction and CO₂ emission reduction.

Supplementary Discussion 2:

The yield stress and Young's modulus for the Al_{0.1}CoCrFeNi systems at 298 K and 1273 K are displayed in tables 1 and 2 of the main text, respectively. The Young's modulus of Al_{0.1}CoCrFeNi from the tensile mechanical tests compares well with the experimental value of 203 GPa and other molecular dynamic simulation values¹⁵⁻¹⁸. The results for the yield stress and strain for the tensile and compression tests also match well with other MD results^{30,31}. For the nanocrystalline systems, it is commonly observed that the Young's modulus decreases with decreasing grain size¹⁹. The compressive Young's modulus for NbMoTaW (Table 3, 4 of the main text) also compares well with experimental data of 318/300 GPa and other simulation values under compression²⁰⁻²². The nanoporous systems display a tension-compression asymmetry that has been reported for other nanoporous systems with tension displaying higher yield strength and young's modulus²³. The asymmetry depends on the type of high entropy alloy and crystal structure as the Al_{0.1}CoCrFeNi nanoporous structure has a higher tensile yield strength compared to its compression, and the NbMoTaW nanoporous system has a higher yield strength under compression. This is consistent with previous reports where the existence of the tension-compression asymmetry results in higher yield strength under tension for fcc materials and higher yield strength under compression for bcc materials²⁴⁻²⁶. This difference can be attributed to the different defect mechanisms that are involved in plastic deformation. For bcc structures, typical defect mechanisms include Peierls stresses for twinning and anti-twinning on the {112} slip planes as well as non-planar core structures

of screw dislocations ²⁶. For fcc structures, the asymmetry is potentially due to biased surface stresses and the different slip planes during tensile and compressive yielding ²⁷

The smaller ligament sizes of the Al_{0.1}CoCrFeNi systems show a lower Young's modulus and yield strength compared to the larger ligaments. Typically, smaller ligament sizes tend to have larger Young's modulus and yield strength. However, smaller ligament sizes beyond a critical ligament size have shown to decrease these values, suggesting that the smaller ligament sizes studied here are smaller than the critical ligament size ²⁸. When the Young's modulus and strength are weight normalized, the high specific strength and low specific modulus are obtained that define the unique properties of the nanoporous HEA as shown in Fig. 1 of the main text.

Supplementary Discussion 3:

A critical consideration when comparing MD results with experimental results is the high strain rate associated with MD simulations that produces higher yield strengths. The discrepancy is particularly evident when comparing bulk gold stress strain calculations in experiments and simulations where MD results show yield strengths around 8.21 GPa whereas experimental values put the yield strength at 205 MPa ^{29,30}. This is particularly true in bulk and nanocrystalline/polycrystalline systems where high strain rates induce different defect mechanisms that contribute to increased strength such as low dislocation density formation. The primary mechanisms that appear to contribute to the high strength in MD simulations are high strain rate as well as small volume size ³¹. However, this appears to be a reduced concern when studying nanoporous materials with bicontinuous structures. MD simulations of nanoporous gold and platinum show excellent agreement with experimental data, even when considering high strain rates, as illustrated in the Gibson-Ashby plot in Fig. 13 ^{24,32-36}. This behavior could be attributed to the ligaments in nanoporous structures behaving similarly to nanowires/pillars, with sizes in the 10s of nm, showing close comparison between simulation and experiment. Theoretical yield strengths of MD simulations align well with expected experimental values that appear to be primarily influenced by nanopillar orientation and size ³⁷. The main disparity between simulation and experimental data is the strain value where yield strength occurs at experimental values lower than MD ³⁷. Considering that the MD simulations conducted in this paper possessing ligaments with sizes less than 10 nm and employed a large simulation with greater than 2,000,000 atoms, it is expected that experimental data with similar parameters would yield similar results.

Supplementary Discussion 4:

Many of the studied nanoporous systems have a fcc crystal structure. The only nanoporous material that is body centered cubic (bcc) is the nanoporous NbMoTaW and W that both have much higher yield strength compared to the other fcc nanoporous systems. This is expected as bcc materials tend to have higher yield strengths due to reduced dislocation motion along slip planes ³⁸. The slip planes of fcc single element metals occur along {110} and {111} planar directions with perfect Burgers vector in the $a/2\langle 110 \rangle$,

which represent close packed directions³⁸. Low stacking fault energies assist in dislocation splitting into partial dislocations which can dissociate onto these close packed planes making slip on these plans relatively easy compared to bcc³⁸. The primary dislocation type in bcc is the screw dislocations that inherently do not have well defined slip planes, reducing the migration of these types of dislocations compared to faster edge dislocations³⁹. The slow screw dislocation movement increases the strength while reducing the ductility of the bcc material⁴⁰. By incorporating nanoporous structures, the brittle nature of bcc materials is addressed by reducing the Young's modulus based on Gibson-Ashby scaling laws⁴¹. This idea of bcc materials having higher strengths can be applied to nanoporous HEA systems that could demonstrate even higher strain hardening compared to single element materials and fcc HEAs that would strengthen individual ligaments. Solid solution strengthening in the bcc HEAs indicates that at low stresses, the common screw and edge dislocations are immobile up to a certain critical stress³⁹. This indicates remarkably high strength at low values of strain. Once the critical stress is reached, both the dislocation types behave similarly with comparably low velocities³⁹. This is quite different to single element bcc materials where screw dislocations are the primary mechanism that controls ductility whereas edge dislocations diffuse much more quickly³⁸. The reduced dislocation motion increases the probability of dislocation-dislocation interactions that may contribute to dislocation multiplication and high strain hardening³⁹. The response to high strain is different depending on which bcc HEA is being examined. The bcc HEA $\text{Co}_{16.67}\text{Fe}_{36.67}\text{Ni}_{16.67}\text{Ti}_{30}$ at high strains shows a transition between jerky motion to smooth gliding dislocations that are similar to other single element bcc materials³⁹. As for the TiZrNbHfTa bcc system, high levels of cross-slipping are shown in fracture analysis that was not observed in the previous bcc HEA that enhances ductility²⁴. This demonstrates that choosing an appropriate bcc HEA is important in reducing the slip mechanism that leads to faster failure of ligaments in a nanoporous system.

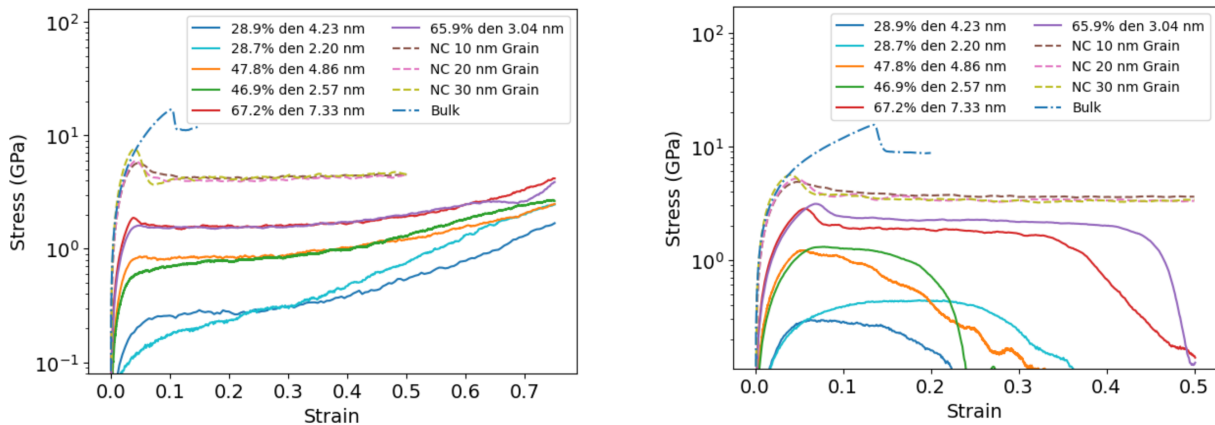


Fig S1. Stress strain curves of tensile and compression tests for $\text{Al}_{0.1}\text{CoCrFeNi}$ systems at 298 K. NC represent nanocrystalline systems (color in print).

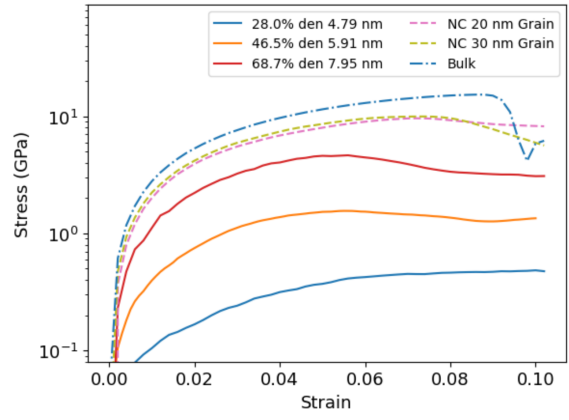
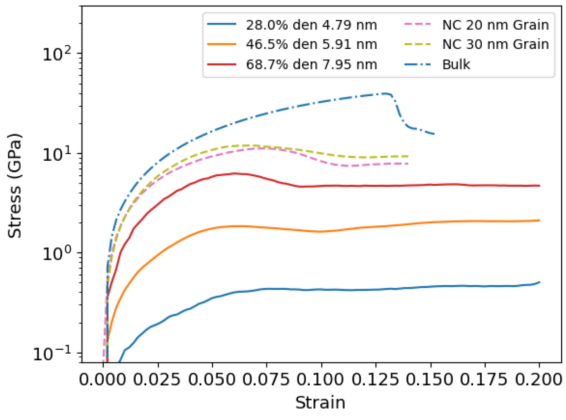
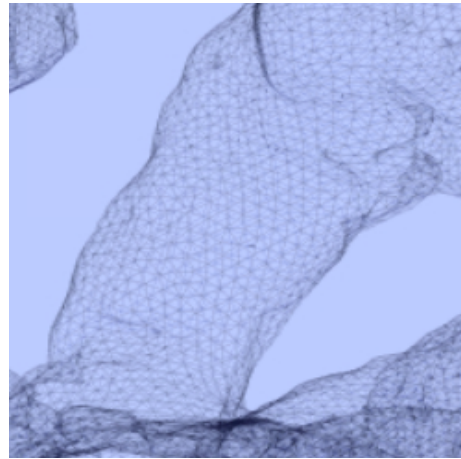
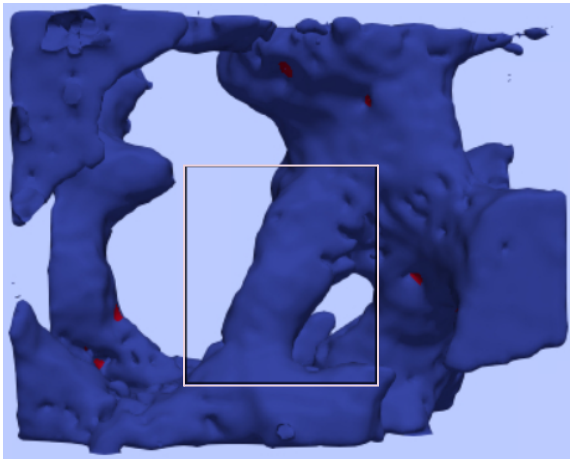


Fig S2. Stress strain curves of compression (left) and tension (right) tests for NbMoTaW systems at 298 K. NC represent nanocrystalline systems (color in print).

a)



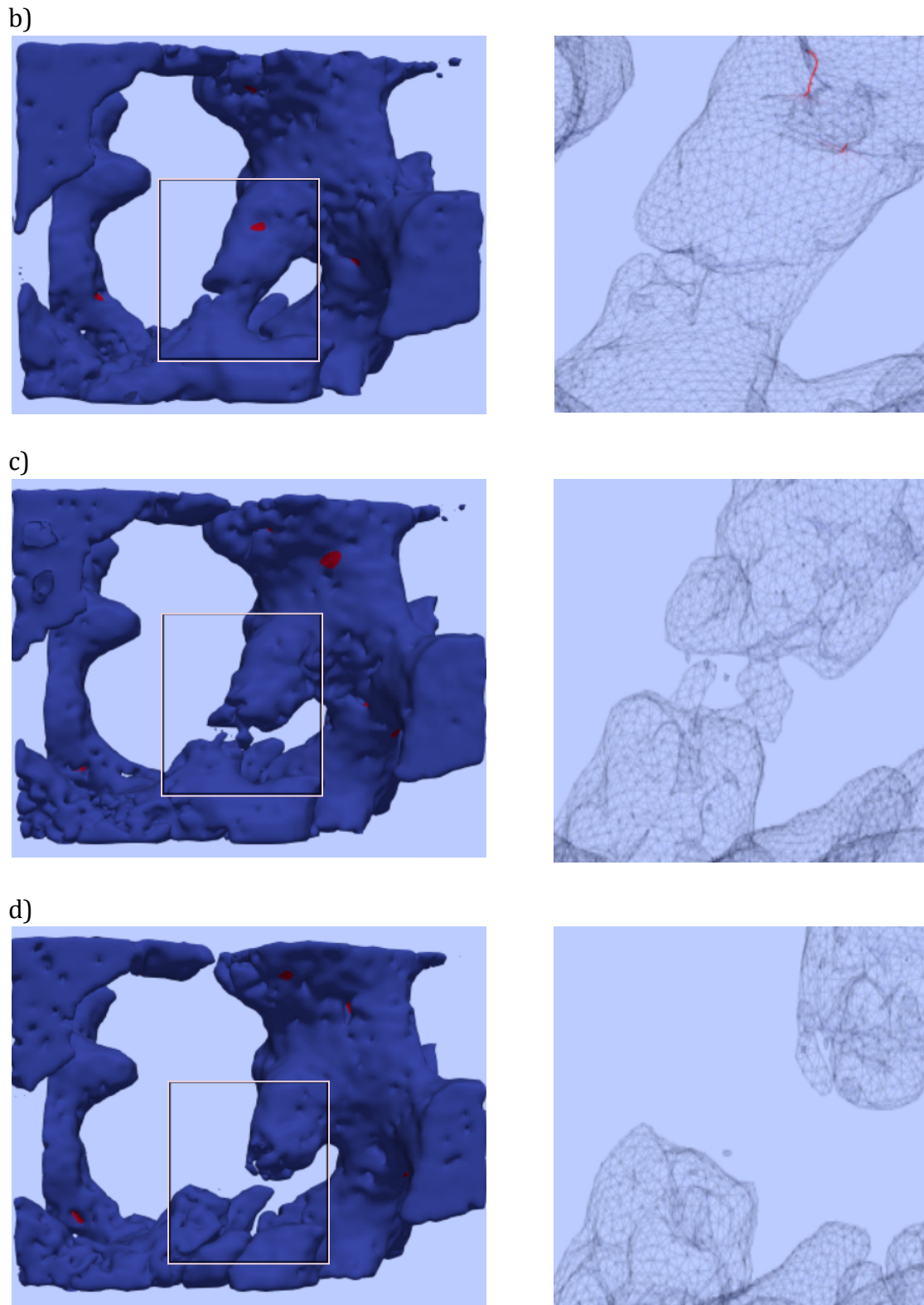


Fig S3. The fracture process of the 28.0% relative density 4.79 nm ligament size nanoporous NbMoTaW HEA under tensile testing. This shows the surface solid mesh outlining the atomic surface and dislocations colored red in the ligament. The strain values

represented are (a) 13.00%, (b) 15.00%, (c) 18.00%, and (d) 20.00%, respectively (color in print)

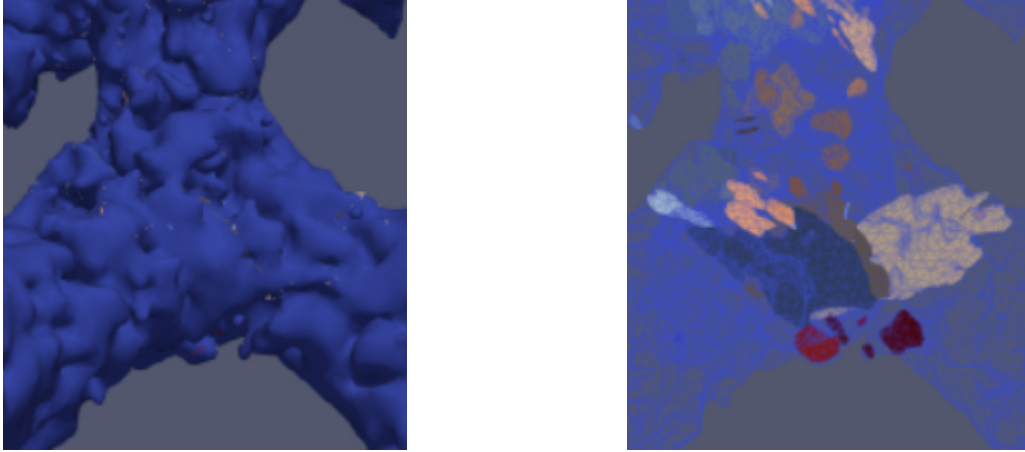


Fig S4. Display of defect pileup in the joints of the NP $\text{Al}_{0.1}\text{CoCrFeNi}$. The image on the left shows the surface of the NP system and the image on the right displays the defects inside the ligament that shows twin boundaries and stacking faults with different colored planes. This is the 28.9% relative density 4.23 nm ligament size nanoporous $\text{Al}_{0.1}\text{CoCrFeNi}$ under tensile testing at 1273 K.

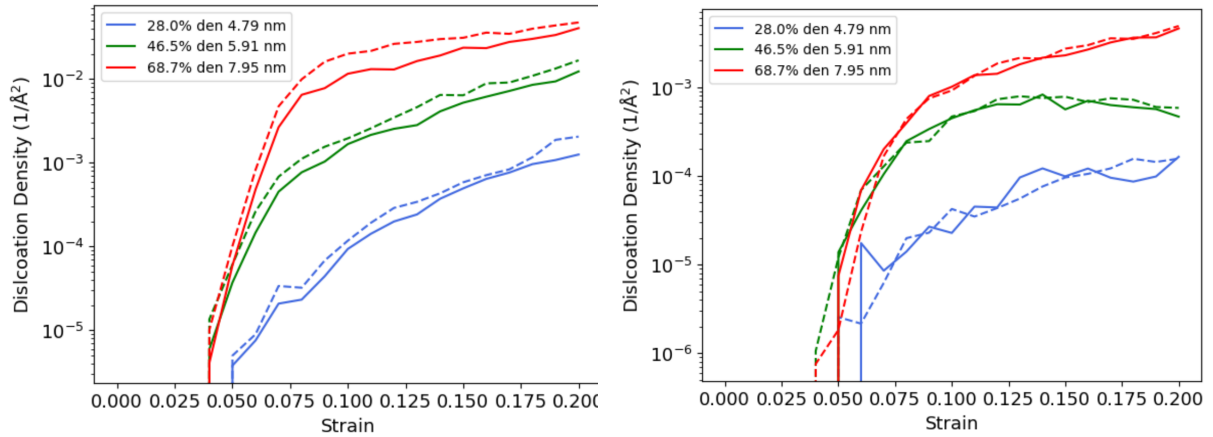


Fig S5. Defect Concentration vs. Strain curves for the NbMoTaW nanoporous systems that focus on dislocations at 600 K (solid line) and 1273 K (dashed line) for compression (left) and tension (right).

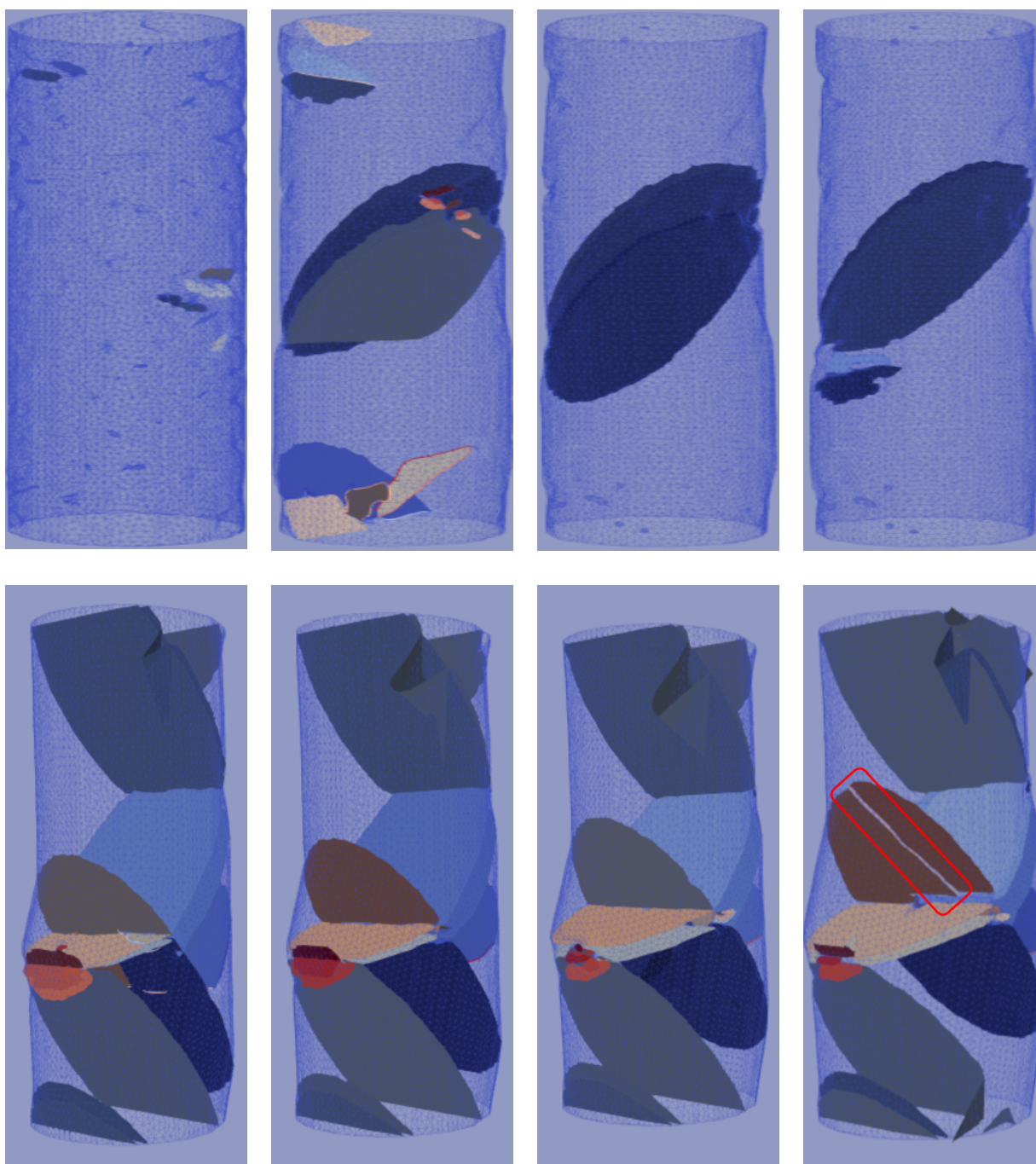


Fig S6. Simulation boxes showing a 7 nm $\text{Al}_{0.1}\text{CoCrFeNi}$ nanopillar under tension (top row) and compression (bottom row) at 298 K at strain values of 13/15/17/19%. The red box corresponds with the partial dislocation outlining the fractured stacking fault (color in print).

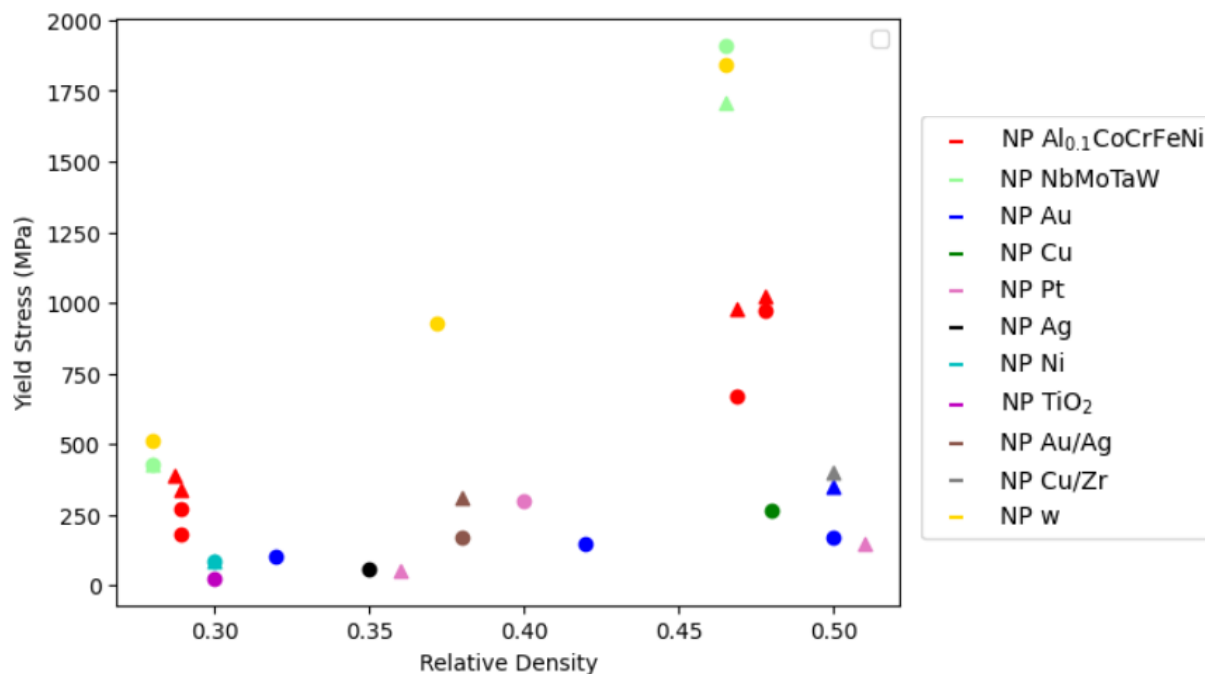


Fig S7. Stress vs. Relative Density of different nanoporous materials given compression (circle) or tensile (triangle) testing. These include nanoporous Al_{0.1}CoCrFeNi, NbMoTaW, Au^{24,32-34}, Cu⁴², Pt^{35,36}, Ag⁴³, Ni⁴⁴, TiO₂⁴⁵, Au/Ag⁴⁶, Cu/Zr⁴⁷, and W (color in print).

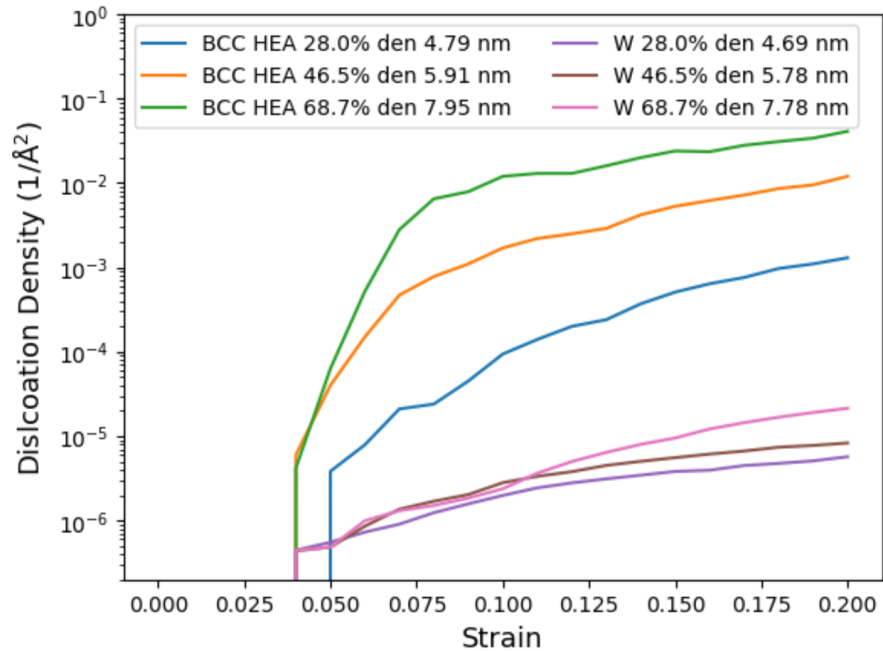


Fig S8. Dislocation Density vs. Strain of Nanoporous NbMoTaW and W under uniaxial compression at 600 K.

References:

1. Thompson, A. P. *et al.* LAMMPS - a flexible simulation tool for particle-based materials modeling at the atomic, meso, and continuum scales. *Comput. Phys. Commun.* **271**, 108171 (2022).
2. Hirel, P. AtomsK: A tool for manipulating and converting atomic data files. *Comput. Phys. Commun.* **197**, 212–219 (2015).
3. Guillotte, M., Godet, J. & Pizzagalli, L. A fully molecular dynamics-based method for modeling nanoporous gold. *Comput. Mater. Sci.* **161**, 135–142 (2019).
4. Daw, M. S. & Baskes, M. I. Semiempirical, Quantum Mechanical Calculation of Hydrogen Embrittlement in Metals. *Phys. Rev. Lett.* **50**, 1285–1288 (1983).
5. Daw, M. S. & Baskes, M. I. Embedded-atom method: Derivation and application to impurities, surfaces, and other defects in metals. *Phys. Rev. B* **29**, 6443–6453 (1984).
6. Chen, Y. *et al.* Development of the interatomic potentials for W-Ta system. *Comput. Mater. Sci.* **163**, 91–99 (2019).
7. Fourmont, A., Le Gallet, S., Politano, O., Desgranges, C. & Baras, F. Effects of planetary ball milling on AlCoCrFeNi high entropy alloys prepared by Spark Plasma Sintering: Experiments and molecular dynamics study. *J. Alloys Compd.* **820**, 153448 (2020).
8. Doan, D.-Q., Fang, T.-H. & Chen, T.-H. Microstructure and composition dependence of mechanical characteristics of nanoimprinted AlCoCrFeNi high-entropy alloys. *Sci. Rep.* **11**, 13680 (2021).
9. Bahramyan, M., Taherzadeh Mousavian, R. & Brabazon, D. Determination of

- atomic-scale structure and compressive behavior of solidified Al_xCrCoFeCuNi high entropy alloys. *Int. J. Mech. Sci.* **171**, 105389 (2020).
10. Li, X.-G., Chen, C., Zheng, H., Zuo, Y. & Ong, S. P. Complex strengthening mechanisms in the NbMoTaW multi-principal element alloy. *Npj Comput. Mater.* **6**, 70 (2020).
 11. Stukowski, A. Dislocation Analysis Tool for Atomistic Simulations. in *Handbook of Materials Modeling* (eds. Andreoni, W. & Yip, S.) 1–14 (Springer International Publishing, 2018). doi:10.1007/978-3-319-42913-7_20-1.
 12. Zhao, D., Wang, Y., Zhang, P. & Liang, D. Modeling and Experimental Research on Resistance Spot Welded Joints for Dual-Phase Steel. *Materials* **12**, 1108 (2019).
 13. Czerwinski, F. Current Trends in Automotive Lightweighting Strategies and Materials. *Materials* **14**, 6631 (2021).
 14. The 2020 EPA Automotive Trends Report Greenhouse Gas Emissions, Fuel Economy, and Technology since 1975. (2021).
 15. Alagarsamy, K. *et al.* Mechanical Properties of High Entropy Alloy Al_{0.1}CoCrFeNi for Peripheral Vascular Stent Application. *Cardiovasc. Eng. Technol.* **7**, 448–454 (2016).
 16. Liu, C., Yang, Y. & Xia, Z. Deformation mechanism in Al_{0.1}CoCrFeNi Σ 3(111)[110] high entropy alloys – molecular dynamics simulations. *RSC Adv.* **10**, 27688–27696 (2020).
 17. Liu, C., Wang, R. & Jian, Z. The Influence of Grain Boundaries on Crystal Structure and Tensile Mechanical Properties of Al_{0.1}CoCrFeNi High-Entropy Alloys Studied by Molecular Dynamics Method. *Crystals* **12**, 48 (2021).
 18. Sharma, A. & Balasubramanian, G. Dislocation dynamics in Al_{0.1}CoCrFeNi high-entropy alloy under tensile loading. *Intermetallics* **91**, 31–34 (2017).
 19. Xia, M., Liu, P. & Sun, Q. Grain size dependence of Young's modulus and hardness for nanocrystalline NiTi shape memory alloy. *Mater. Lett.* **211**, 352–355 (2018).
 20. Xu, J. *et al.* Enhanced strength and ductility of laser powder bed fused NbMoTaW refractory high-entropy alloy via carbon microalloying. *Addit. Manuf. Lett.* **3**, 100079 (2022).
 21. Clark, P. Computation Aided Design Of Multicomponent Refractory Alloys With A Focus On Mechanical Properties. (University of Mississippi, 2016).
 22. Hu, Y. L. *et al.* First-principle calculation investigation of NbMoTaW based refractory high entropy alloys. *J. Alloys Compd.* **827**, 153963 (2020).
 23. Joseph, J., Stanford, N., Hodgson, P. & Fabijanic, D. M. Tension/compression asymmetry in additive manufactured face centered cubic high entropy alloy. *Scr. Mater.* **129**, 30–34 (2017).
 24. Saffarini, M. H., Voyiadjis, G. Z. & Ruestes, C. J. Temperature effect on nanoporous gold under uniaxial tension and compression. *Comput. Mater. Sci.* **200**, 110766 (2021).
 25. Jeon, H., Lee, S. & Kim, J.-Y. Tension-compression asymmetry in plasticity of nanoporous gold. *Acta Mater.* **199**, 340–351 (2020).
 26. Yilmaz, H. Mechanical Properties of Body-Centred Cubic Nanopillars. (University of Manchester, 2018).
 27. Diao, J., Gall, K. & Dunn, M. L. Yield Strength Asymmetry in Metal Nanowires. *Nano Lett.* **4**, 1863–1867 (2004).
 28. Giri, A., Tao, J., Wang, L., Kirca, M. & To, A. C. Compressive Behavior and Deformation Mechanism of Nanoporous Open-Cell Foam with Ultrathin Ligaments. *J. Nanomechanics Micromechanics* **4**, A4013012 (2014).
 29. Son, S.-B. *et al.* Relationship between microstructure homogeneity and bonding stability

- of ultrafine gold wire. *Gold Bull.* **44**, (2011).
30. Deng, C. & Sansoz, F. Uniaxial Compression Behavior of Bulk Nano-twinned Gold from Molecular Dynamics Simulation. *MRS Proc.* **1049**, (2007).
 31. Koyanagi, J., Takase, N., Mori, K. & Sakai, T. Molecular dynamics simulation for the quantitative prediction of experimental tensile strength of a polymer material. *Compos. Part C Open Access* **2**, 100041 (2020).
 32. Kim, Y.-C. *et al.* Indentation size effect in nanoporous gold. *Acta Mater.* **138**, 52–60 (2017).
 33. Biener, J., Hodge, A. M., Hamza, A. V., Hsiung, L. M. & Satcher, J. H. Nanoporous Au: A high yield strength material. *J. Appl. Phys.* **97**, 024301 (2005).
 34. Przybilla, T. Studying the Structure and Mechanical Properties of Nanoporous Materials by Advanced Tomography and in Situ Mechanical Testing. (2019).
 35. Liu, R., Gruber, J., Bhattacharyya, D., Tucker, G. J. & Antoniou, A. Mechanical properties of nanocrystalline nanoporous platinum. *Acta Mater.* **103**, 624–632 (2016).
 36. Xian, Y., Li, J., Wu, R. & Xia, R. Softening of nanocrystalline nanoporous platinum: A molecular dynamics simulation. *Comput. Mater. Sci.* **143**, 163–169 (2018).
 37. Wang, S., Shan, Z. & Huang, H. The Mechanical Properties of Nanowires. *Adv. Sci.* **4**, 1600332 (2017).
 38. Weinberger, C. R., Boyce, B. L. & Battaile, C. C. Slip planes in bcc transition metals. *Int. Mater. Rev.* **58**, 296–314 (2013).
 39. Chen, B. *et al.* Unusual activated processes controlling dislocation motion in body-centered-cubic high-entropy alloys. *Proc. Natl. Acad. Sci.* **117**, 16199–16206 (2020).
 40. Zhou, X., He, S. & Marian, J. Cross-kinks control screw dislocation strength in equiatomic bcc refractory alloys. *Acta Mater.* **211**, 116875 (2021).
 41. Gibson, L. J. & Ashby, M. F. *Cellular solids: structure and properties*. (CUP, 1999).
 42. Liu, R. *et al.* In situ frustum indentation of nanoporous copper thin films. *Int. J. Plast.* **98**, 139–155 (2017).
 43. Li, Z. & Lu, X. Nanoindentation for mechanical behaviour characterization of nanoporous silver fabricated through dealloying. *Bull. Mater. Sci.* **44**, 149 (2021).
 44. Kashani, H. & Chen, M. Flaw-free nanoporous Ni for tensile properties. *Acta Mater.* **166**, 402–412 (2019).
 45. Lee, J.-H., Kim, H.-E., Shin, K.-H. & Koh, Y.-H. Improving the strength and biocompatibility of porous titanium scaffolds by creating elongated pores coated with a bioactive, nanoporous TiO₂ layer. *Mater. Lett.* **64**, 2526–2529 (2010).
 46. Beets, N., Farkas, D. & Albe, K. The Mechanical Response of Nanoporous Gold and Silver Foams with Varying Composition and Surface Segregation. *Acta Mater.* **203**, 116445 (2021).
 47. Liu, C., Yuan, S. & Branicio, P. S. Bicontinuous nanoporous design induced homogenization of strain localization in metallic glasses. *Scr. Mater.* **192**, 67–72 (2021).